Control of Ti1-xSixN nanostructure via tunable metal-ion momentum transfer during HIPIMS/DCMS co-deposition

Grzegorz Greczynski, J. Patscheider, Jun Lu, Björn Alling, Annop Ektarawong, Jens Jensen, Ivan Petrov, Joseph E Greene and Lars Hultman

Linköping University Post Print

N.B.: When citing this work, cite the original article.

Original Publication:

Grzegorz Greczynski, J. Patscheider, Jun Lu, Björn Alling, Annop Ektarawong, Jens Jensen, Ivan Petrov, Joseph E Greene and Lars Hultman, Control of Ti1-xSixN nanostructure via tunable metal-ion momentum transfer during HIPIMS/DCMS co-deposition, 2015, Surface & Coatings Technology, (280), 174-184.
http://dx.doi.org/10.1016/j.surfcoat.2015.09.001
Copyright: Elsevier
http://www.elsevier.com/

Postprint available at: Linköping University Electronic Press
http://urn.kb.se/resolve?urn=urn:nbn:se:liu:diva-122787

Control of $Ti_{1-x}Si_xN$ nanostructure via tunable metal-ion momentum transfer during HIPIMS/DCMS co-deposition

G. Greczynski,[1,*] J. Patscheider,[2] J. Lu,[1] B. Alling,[1,3] A. Ektarawong,[1] J. Jensen,[1]
I. Petrov,[1,4] J. E. Greene,[1,4] L. Hultman[1]

[1] *Thin Film Physics Division, Department of Physics (IFM), Linköping University, SE-581 83 Linköping, Sweden*
[2] *Laboratory of Nanoscale Materials Science, Empa, Überlandstr. 129, 8600 Dübendorf, Switzerland*
[3] *Max-Planck-Institut für Eisenforschung GmbH, D-40237 Düsseldorf, Germany*
[4] *Materials Science and Physics Departments and the Frederick Seitz Materials Research Laboratory, University of Illinois, Urbana, Illinois 61801*

* - corresponding author (grzgr@ifm.liu.se; phone: +46 13 281213)

Abstract

$Ti_{1-x}Si_xN$ ($0 \leq x \leq 0.26$) thin films are grown in mixed Ar/N_2 discharges using hybrid high-power pulsed and dc magnetron co-sputtering (HIPIMS/DCMS). In the first set of experiments, the Si target is powered in HIPIMS mode and the Ti target in DCMS; the positions of the targets are then switched for the second set. In both cases, the Si concentration in co-sputtered films, deposited at T_s = 500 °C, is controlled by adjusting the average DCMS target power. A pulsed substrate bias of –60 V is applied in synchronous with the HIPIMS pulse. Depending on the type of pulsed metal-ion irradiation incident at the growing film, Ti^+/Ti^{2+} *vs.* Si^+/Si^{2+}, completely different nanostructures are obtained. Ti^+/Ti^{2+} irradiation during Ti-HIPIMS/Si-DCMS deposition leads to a phase-segregated nanocolumnar structure with TiN-rich grains encapsulated in a SiN_z tissue phase, while Si^+/Si^{2+} ion irradiation in the Si-HIPIMS/Ti-DCMS mode results in the formation of $Ti_{1-x}Si_xN$ solid solutions with $x \leq 0.24$. Film properties, including hardness, modulus of elasticity, and residual stress exhibit a dramatic dependence on the choice of target powered by HIPIMS. Ti-HIPIMS/Si-DCMS TiSiN nanocomposite films are superhard over a composition range, $0.04 \leq x \leq 0.26$, that is significantly wider than previously reported. The hardness H of films with $0.13 \leq x \leq 0.26$ is ~42 GPa; however, the compressive stress is also high, ranging from -6.7

to -8.5 GPa. Si-HIPIMS/Ti-DCMS films are softer, $H \sim 14$ GPa with $0.03 \leq x \leq 0.24$, and essentially stress-free (σ ~0.5 GPa). Mass spectroscopy analyses at the substrate position reveal that the doubly-to-singly ionized metal-ion flux ratio during HIPIMS pulses is 0.05 for Si and 0.29 for Ti due to the difference between the second ionization potentials of Si and Ti *vs*. the first ionization potential of the sputtering gas. The average momentum transfer to the film growth surface per deposited atom per pulse $\langle p_d \rangle$ is ~20× higher during Ti-HIPIMS/Si-DCMS, which results in significantly higher adatom mean-free paths (mfps) leading, in turn, to a phase-segregated nanocolumnar structure. In contrast, relatively low $\langle p_d \rangle$ values during Si-HIPIMS/Ti-DCMS provides near-surface mixing with lower adatom mfps to form $Ti_{1-x}Si_xN$ solid solutions over a very wide composition range with x up to 0.24. Relaxed lattice constants decrease linearly, in agreement with *ab-initio* calculations for random $Ti_{1-x}Si_xN$ alloys, with increasing x.

1. Introduction

Low-energy inert-gas ion irradiation of the film surface during refractory transition-metal (TM) nitride growth by conventional DC magnetron sputtering has been used extensively to overcome the characteristically underdense microstructures with rough surfaces of layers deposited at low temperatures ($T_s / T_m < 0.30$, in which T_s is the film growth temperature and T_m is the melting point in K).[1] High-flux, low-energy ion bombardment has been shown to increase nucleation rates[2,3,4] and film density,[4] give rise to renucleation which inhibits the formation of open columnar microstructures associated with high surface roughness,[5,6] reduce defect density,[7] and control preferred orientation.[1,8,9,10] However, the balance is delicate and at higher ion energies, a steep price is extracted in the form of residual ion-induced compressive stress resulting from both recoil implantation of surface atoms and trapping of rare-gas ions in the lattice.[11,12,13]

We recently demonstrated that high-power pulsed magnetron sputtering (HIPIMS) provides an alternative route for ion-assisted TM nitride film growth via the use of substrate bias synchronized to the *metal-rich* portion of the plasma pulse. Stresses can be dramatically reduced, or even eliminated, since *metal* (as opposed to inert-gas) ions are components of the film.[14,15] In those experiments, we used metastable NaCl-structure $Ti_{1-x}Al_xN$,[16,17] known to be very sensitive to ion-irradiation-induced phase separation, as a model system deposited in a hybrid high-power pulsed and dc magnetron (HIPIMS/DCMS) co-sputtering configuration to show that the average metal-ion momentum $\langle p_d \rangle$ per deposited atom, rather than the average metal-ion energy $\langle E_d \rangle$ as previously proposed,[18,19] controls film phase composition and stress evolution.[16,20] With $\langle p_d \rangle > \langle p_d^* \rangle \simeq 135$ [eV-amu]$^{1/2}$, as-deposited $Ti_{1-x}Al_xN$ films are two-phase mixtures. In addition, film-growth pathways are distinctly different depending upon which

target, Ti or Al, is powered by HIPIMS.[16,17,21] $\langle p_d^* \rangle$ is exceeded during Ti-HIPIMS, even with no intentional applied substrate bias, due to the combined higher mass and average charge state of Ti^{n+} ions (n = 1,2), resulting in films with low hardness (~18 GPa) and high compressive stress, up to -2.7 GPa.[16] In contrast, with Al^{n+} ion irradiation of the growing film, in which the fraction of ions with $n > 1$ is negligible, during Al-HIPIMS/Ti-DCMS with the synchronous substrate bias V_s varied from 20 to 160 V, the hardness of single-phase NaCl-structure $Ti_{0.38}Al_{0.62}N$ alloys increases from 12 to 31 GPa while the residual stress σ remains ~ 0.[20]

Here, we use hybrid HIPIMS/DCMS co-sputtering to explore synchronous metal-ion irradiation effects on phase-composition in the $Ti_{1-x}Si_xN$ system. Momentum transfer due to ion irradiation of the growing film is expected to be similar to that of $Ti_{1-x}Al_xN$ due to the close mass match between Al (26.98 amu) and Si (28.09 amu). However, $Ti_{1-x}Si_xN$ represents a much more stringent test of hybrid HIPIMS/DCMS film growth with synchronous bias since the reported metastable NaCl-structure solid-solution range, $x_{max} \leq 0.09$, for films grown by cathodic-arc evaporation is quite narrow.[22] In the special case of ultra-thin epitaxial $Ti_{1-x}Si_xN(001)$ films grown by reactive magnetron sputtering on TiN(001), Si was substitutionally incorporated on cation sites with $x \leq 0.19$.[23] However, the thickness of such layers is limited to a few tens of nm. For comparison, the equilibrium phase diagram exhibits no solid solution at all.

The TiN/SiN_x system has been widely studied[24,23,25,26] for the synthesis of superhard (H > 40 GPa)[27] nanocomposite thin films, with the primary applications being wear-resistant coatings on cutting tools, based upon phase self-organization during film growth. The first report on nanocomposite hardness enhancement, by Li Shizhi et al.,[28] was followed by a series of papers by Veprek et al.[27,29,30] exploiting high-temperature film growth to provide strong SiN_z

surface segregation giving rise to a nanostructure consisting of TiN crystallites encapsulated by a few monolayers (ML) of a disordered SiN_z tissue phase.[25] This occurs dynamically as SiN_z segregation to the surface of TiN-rich grains forces TiN, which segregates in turn to the surface of the SiN_z layer, to renucleate.[31] The stepwise process is repeated throughout film growth, thus eliminating columnar formation with associated underdense intracolumnar boundaries and giving rise to very smooth surfaces. The encapsulation layers also constrain further growth of the TiN nanograins. Hultman et al.[25] later showed that the initial SiN monolayers grow with local epitaxy on TiN crystallites before forming disordered Si_3N_4 due to bond strain, as Si atoms prefer to be tetrahedrally coordinated with an oxidation state of +4. For nanocomposite films grown by plasma-assisted chemical vapor deposition (PA-CVD) and by reactive magnetically unbalanced magnetron sputter deposition, the maximum $Ti_{1-x}Si_xN$ hardness is typically achieved with SiN contents x in the range $0.14 \leq x \leq 0.20$.[23,30,25,32,33,34]

Reactive cathodic-arc evaporation from Ti and Ti/Si cathodes has been used to deposit $Ti_{1-x}Si_xN$ layers at 500°C. The films have hardness values up to 44.7±1.9 GPa for $x = 0.14$ and exhibit a very fine, defect-rich, feather-like nanostructure consisting of TiN columns with average widths less than 10 nm.[35] The authors reported no indication of an amorphous phase and noted that the $Ti_{1-x}Si_xN$ films were stable up to at least 900°C without phase segregation or softening. However, their XRD results show significant peak broadening as x is increased from 0 to 0.14 which, together with the fact that film lattice parameters remain constant at the original TiN value, indicates that the layers are phase separated.

In addition to $Ti_{1-x}Si_xN$ solid-solution, the system may also separate into its cubic components. TiN/SiN_z interfaces have thus also been studied using first-principles calculations. The results highlight the importance of considering lattice dynamics,[36,37,38] the stoichiometry of

the SiN_z tissue phase,[39,40] and the coordination of Si atoms,[41] as these factors influence bond strengths across the interfaces.

In the present experiments, we use a hybrid HIPIMS/DCMS film growth technique[16,17,21] to investigate the effects of Ti^{n+} *vs*. Si^{n+} metal-ion irradiation on the properties of $Ti_{1-x}Si_xN$ layers. Depending on the choice of metal ions, completely different nanostructures are obtained. Ti^+/Ti^{2+} irradiation leads to a phase-separated structure consisting of TiN-rich nanocolumns encapsulated in SiN_z tissue phases, while Si^+/Si^{2+} metal-ion irradiation results in the formation of $Ti_{1-x}Si_xN$ solid solution alloys with $x \leq 0.24$. As a consequence, film properties, including hardness, modulus of elasticity, and residual stress exhibit dramatic dependences on the choice of target, Si or Ti, powered by HIPIMS. Ti-HIPIMS/Si-DCMS $Ti_{1-x}Si_xN$ films are superhard two-phase nanocomposites, with H varying from 39 to 45 GPa, over a composition range, $0.04 \leq x \leq 0.26$, that is significantly wider than reported previously. However, the compressive stress is also high, ranging from -4.5 to -8.5 GPa. Si-HIPIMS/Ti-DCMS single-phase solid-solution alloy films are softer, with $H \sim 14$ GPa over the entire composition range investigated, $0.03 \leq x \leq 0.24$, and are essentially stress-free ($\sigma \sim 0.5$ GPa).

2. Experimental procedures

2.1. Film growth

$Ti_{1-x}Si_xN$ films are grown in a multi-target CemeCon AG CC800/9 magnetron sputtering system.[42] The Ti and Si targets are cast rectangular plates with dimensions 8.8×50 cm². Si(001) substrates, 2×1 cm^2, are positioned symmetrically with respect to the targets, which are tilted toward the substrate. The angle between the substrate normal and lines connecting the centers of the targets with the centers of the substrates is 21°, and the target-to-substrate distance is 18 cm. Substrates are cleaned sequentially in acetone and isopropanol alcohol and mounted with

clips such that their long sides are parallel to the long sides of the targets. The system base pressure is < 0.3 mPa (2.3×10^{-6} Torr), and the total pressure P_{tot} during deposition is 0.4 Pa (3 mTorr) with a N_2/Ar flow ratio of 0.2. Substrate temperature T_s during deposition is 500 °C. Heating is accomplished using resistance heaters mounted symmetrically on the front and back sides of the vacuum chamber. Power to each heater is 10 kW during the 2 h preheating cycle and 8 kW during the 1.5 h depositions.

A hybrid deposition scheme is employed in which one of the targets is operated in HIPIMS mode at constant pulse energy and duty cycle, while the other is operated as a conventional magnetron with varying dc power. Two series of film growth experiments are carried out. In the first set, the Ti target is operated in HIPIMS mode and dc power is applied to the Si target (Ti-HIPIMS/Si-DCMS). The positions of the targets are then switched for the second series of experiments (Si-HIPIMS/Ti-DCMS). To allow direct comparison between the two sets of films, the energy per HIPIMS pulse is maintained constant. HIPIMS pulse frequency and DCMS power are varied to control film compositions. In the Ti-HIPIMS/Si-DCMS configuration, the average HIPIMS power $\mathscr{P}_{HIPIMS}$ is 5 kW (10 J/pulse, 500 Hz, 10% duty cycle), while the DCMS power $\mathscr{P}_{dc}$(Si target) is varied from 0 to 0.4 kW resulting in $Ti_{1-x}Si_xN_y$ compositions ranging from 0 to 26 mole% SiN. For the second set of experiments, carried out in the Si-HIPIMS/Ti-DCMS mode, $\mathscr{P}_{HIPIMS}$ = 1 kW (10 J/pulse, 100 Hz, 2% duty cycle) with $\mathscr{P}_{dc}$ varied from 10 to 4 kW providing $Ti_{1-x}Si_xN_y$ films with x = 0.03 to 0.24. In addition, DCMS TiN films (x = 0) are grown, for reference, in the same configuration by setting $\mathscr{P}_{HIPIMS}$ = 0 kW with $\mathscr{P}_{dc}$ = 6 kW. The higher power used during Ti-HIPIMS is primarily due to the higher degree of Ti metal ionization resulting in a larger fraction of sputter-ejected metal atoms accelerated

back to the target.[43,44] The growth rate R during Ti-HIPIMS/Si-DCMS varies from 4 nm/min with $\mathcal{P}_{dc}^{Si}$ = 0.2 kW to 5.4 nm/min with $\mathcal{P}_{dc}^{Si}$ = 0.4 kW, whereas during Si-HIPIMS/Ti-DCMS, R is 26.6 nm/min with $\mathcal{P}_{dc}^{Ti}$ = 4 kW and increases to 56.9 nm/min with $\mathcal{P}_{dc}^{Ti}$ = 10 kW. A pulsed substrate bias, V_s = -60 V, synchronized to the HIPIMS pulse, is used in all experiments. Between HIPIMS pulses, the substrate is at floating potential, V_f = -10 V. Target current and voltage waveforms during film growth are recorded with a Tektronix 500 MHz bandwidth digital oscilloscope.

2.2. In-situ ion-flux analyses

A Hiden Analytical EQP1000 mass spectrometer is used for *in-situ* time-dependent measurements of the compositions and energies of ion fluxes incident at the substrate plane for each target configuration. In these experiments, the axis of the mass spectrometer is placed perpendicular to, and 18 cm from, each target surface, corresponding to the target/substrate distance during film growth.[45] Ion-energy-distribution functions (IEDFs) are recorded in HIPIMS mode while sputtering in Ar/N_2 at P_{tot} = 0.4 Pa (3 mTorr). For the Si target, IEDFs are acquired for Ar^+, Ar^{2+}, Si^+, and Si^{2+} ions in time-resolved HIPIMS modes. Corresponding results for Ar^+, Ar^{2+}, Ti^+, and Ti^{2+} are obtained with the Ti target. The ion energy E_i is scanned in 1 eV steps over the range $1 \leq E_i \leq 30$ eV. The contribution of ions with $E_i > 30$ eV to the integrated ion flux is less than 1%. The average ion energy $\langle E \rangle_{M^{n+}}$ of M^{n+}ions, in which M is the metal species and n is the charge state, is a weighted average calculated from the measured ion intensity $I_{M^{n+}}(E_i)$ in the corresponding ion energy distribution function:

$$\langle E \rangle_{M^{n+}} = \frac{\int_{E_i=1}^{E_i=E_i'} I_{M^{n+}}(E_i) E_i dE_i}{\int_{E_i=1}^{E_i=E_i'} I_{M^{n+}}(E_i) dE_i}. \quad (1)$$

2.3. Film characterization

$Ti_{1-x}Si_xN_y$ film compositions are determined by time-of-flight elastic recoil detection analyses (ToF ERDA),[46] to within a measurement accuracy of ±0.005, at the Uppsala University tandem accelerator. A 36 MeV $^{127}I^{8+}$ probe beam is incident at 67.5° with respect to the sample surface normal; recoils are detected at 45°. Film thicknesses are obtained from cross-sectional scanning electron microscopy (SEM) analyses in a LEO 1550 instrument.

θ-2θ x-ray diffraction (XRD) scans, in steps of 0.1°, and $\sin^2\psi$ measurements for residual stress determinations,[47] are carried out using a Philips X'Pert MRD system operated with point-focus Cu Kα radiation. In the $\sin^2\psi$ technique,[47] film strain ε is evaluated by measuring the position of a Bragg reflection to obtain the corresponding film interplanar spacing d as a function of the tilt angle ψ between the sample normal and the scattering plane defined by the incoming and diffracted x-ray beams. The tilt-angle resolved film strain $\varepsilon(\psi)$, defined with respect to the substrate normal, is equal to the normalized difference between d and the relaxed interplanar spacing d_o,

$$\varepsilon(\psi) = \frac{d - d_o}{d_o} . \qquad (2)$$

Measured $\varepsilon(\psi)$ values are used to determine the residual stress σ through Hooke's law of linear elasticity as[47]

$$\varepsilon(\psi) = \frac{1+\upsilon}{E}\sigma sin^2\psi - \frac{2\upsilon}{E}\sigma , \qquad (3)$$

where ν is Poisson's ratio and E is the elastic modulus. Experimentally, the in-plane stress is extracted from the slope of $\varepsilon(\psi)$ *vs*. $\sin^2\psi$.

Relaxed $Ti_{1-x}Si_xN$ lattice constants a_o are determined as a function of x from θ–2θ scans acquired at the strain-free tilt angle ψ^*, defined by setting $\varepsilon = 0$ in Eq. (3):

$$\psi^* = arcsin\left(\sqrt{\frac{2\nu}{1+\nu}}\right). \tag{4}$$

While $\nu(x)$ is unknown for $Ti_{1-x}Si_xN$, ν ranges only from 0.27 for Si_3N_4 to 0.25 for TiN. Variation in ν over this range changes ψ^* by less than ±1°. Here, we use $\nu = 0.26$ which yields $\psi^* = 40.0°$.

Film preferred orientations are obtained from integrated XRD peak intensities I_{hkl} normalized to corresponding results from powder diffraction patterns. The degree of 111 texture in films exhibiting both 111 and 002 diffraction peaks is expressed as $I_{111}/(I_{111} + I_{002})$.

A Berkovich diamond tip is used to determine nanoindentation hardnesses H and elastic moduli E of as-deposited $Ti_{1-x}Si_xN$ films as a function of x. A minimum of 20 indents, with a maximum load of 15 mN, are made in each sample. Indentation depths range from 1500 to 2000 Å, but are never allowed to exceed 10% of the film thickness in order to minimize substrate effects. Results are analyzed using the method of Oliver and Pharr.[48]

Samples for plan-view transmission electron microscopy (TEM), plan-view scanning TEM (STEM), cross-sectional TEM (XTEM), and energy-dispersive spectroscopy (EDX) analyses are prepared by mechanical polishing, followed by Ar^+ ion milling at 5 kV with an 8° incidence angle and sample rotation. During the final thinning stages, the ion energy and incidence angle are reduced to 2.5 kV and 5°. Film microstructure is analyzed in an FEI Tecnai G2 TF 20 UT transmission electron microscope operated at 200 kV. The EDX mapping and high resolution STEM (HRSTEM) images are obtained with a double-C_s-corrected FEI Titan[3] 60–300 microscope operated at 300 kV and equipped with the Super-X EDX detector.

X-ray photoelectron spectroscopy (XPS) valence-band spectra are acquired from air-exposed $Ti_{1-x}Si_xN$ films in a Kratos Analytical instrument, with a base pressure of 1.5×10^{-7} Pa (1.1×10^{-9} Torr), using monochromatic Al Kα radiation (hν = 1486.6 eV). Prior to analysis, film surfaces are sputter-etched *in-situ* using 0.5 keV Ar^+ ions incident at an angle of 70° with respect to the surface normal. The ion current density is 9.5 mA/cm^2, and the beam is rastered over a 3×3 mm^2 area for 5 min, corresponding to the removal of ~50 Å from a polycrystalline Ta_2O_5 reference sample.

TRIM (Transport of Ions in Matter),[49] a Monte Carlo program included in the SRIM (Stopping power and Range of Ions in Matter) software package,[50] is used to estimate thicknesses d_{Ar} of $Ti_{1-x}Si_xN$ layers modified by Ar^+ bombardment during sample preparation for XPS analyses. d_{Ar}, the sum of the projected average surface-atom recoil range and straggle, for collision cascades induced by 0.5 keV Ar^+ ions incident on $Ti_{1-x}Si_xN$ surfaces ($0 \leq x \leq 0.26$) at an angle of 70°, does not exceed 1 nm, whereas the XPS probing depth (film thickness corresponding to 95% of the signal intensity) is ~9 nm. Thus, the majority of the XPS signal intensity originates from the unmodified layer.

3. Computational details

$Ti_{1-x}Si_xN$ lattice parameters as a function of x are obtained using first-principles calculations performed within density functional theory and the Projector Augmented Wave method[51] as implemented in the Vienna Ab-Initio Simulation Package (VASP)[52,53] using the generalized gradient approximation (GGA)[54] to account for electron exchange-correlation effects. Supercells consist of 216 atoms, based on 3×3×3 repetitions of the conventional NaCl-structure unit cell. Alloy compositions are x = 0, 0.056, 0.111, 0.167, and 0.25 in $Ti_{1-x}Si_xN$ random alloys

with the atomic configurations constructed using the special quasi-random structure method (SQS)[55] following the procedure described in Ref. 56 for $Ti_{1-x}Al_xN$ alloys.

To determine elastic properties, strains ϵ with $\pm1\%$ and $\pm2\%$ distortions are applied to the relaxed $Ti_{1-x}Si_xN$ supercells without volume conservation. In order to avoid residual stresses, the lattice parameters as well as the internal atomic coordinates are relaxed such that pressures are always less than 10^6 Pa. The elastic constants of $Ti_{1-x}Si_xN$ are then calculated using the second-order Taylor expansion of the total energy,

$$C_{ij} = \frac{1}{V_0} \frac{\partial^2 E(\epsilon_1,\dots,\epsilon_6)}{\partial \epsilon_i \partial \epsilon_j}\bigg|_0, \tag{5}$$

in which Voigt's notation is used to describe the strain ϵ and elastic tensor C_{ij}.[57,58] $E(\epsilon_1, \dots, \epsilon_6)$ is defined as the total energy of the distorted supercell due to the correspondingly applied strain; V_0 is the equilibrium volume of the undistorted supercell. Since the SQS approach generally breaks the point-group symmetry for alloy systems, the elastic constants are cube-averaged[59] and nine independent elastic constants -- C_{11}, C_{12}, C_{13}, C_{22}, C_{23}, C_{33}, C_{44}, C_{55}, and C_{66} -- are calculated. The three elastic constants of $Ti_{1-x}Si_xN$ in the NaCl-structure are obtained as

$$\overline{C}_{11} = \frac{C_{11}+C_{22}+C_{33}}{3}, \ \overline{C}_{12} = \frac{C_{12}+C_{13}+C_{23}}{3}, \ \overline{C}_{44} = \frac{C_{44}+C_{55}+C_{66}}{3}. \tag{6}$$

Isotropic $Ti_{1-x}Si_xN$ Young's moduli are obtained using the Voigt-Reuss-Hill (VRH) approach[60] for determining elastic properties of polycrystalline solids

Results

4.1. Discharge characteristics

Figure 1 shows target voltage, current, and power density waveforms recorded during 200-μs HIPIMS pulses in Ti-HIPIMS/Si-DCMS and Si-HIPIMS/Ti-DCMS deposition modes. For Ti-HIPIMS, the target voltage $V_T(t)$ is 610 V at $t = 0$ and decreases, due to the size of the

capacitor bank with respect to the target area, to saturate at 170 V at t = 100 μs. Following plasma ignition at t = 5 μs, the target current $J_T(t)$, Fig. 1(b), increases rapidly to a maximum value of 1.11 A/cm^2 at 35 μs, and then decreases more gradually to essentially zero at ~120 μs as $V_T(t)$ becomes too low to sustain the discharge. Thus, the effective discharge pulse length is reduced to ~110 μs. The target power density $\mathscr{P}_T(t)$, Fig. 1(c), also increases rapidly after plasma ignition to 473 W/cm^2 at t = 30 μs and decreases thereafter to effectively zero at t ~120 μs.

For Si-HIPIMS, $V_T(t)$ is significantly higher, 780 V at t = 0, and decreases to saturate at 480 V with t = 150-200 μs. The rate of the initial Si-HIPIMS voltage decrease is approximately 3× less than for the case of Ti-HIPIMS. $J_T(t)$ increases rapidly after plasma ignition, t = 5 μs, and reaches a maximum of 0.38 A/cm^2 at 70 μs. However, in contrast to Ti-HIPIMS, $J_T(t)$ does not drop to zero, but saturates at ~0.02 A/cm^2, a level typical of DCMS discharges, for t > 160 μs.[61,62] $\mathscr{P}_T(t)$ exhibits an initial increase, Fig. 1(c), following the behavior of $J_T(t)$, to reach a peak value of 233 W/cm^2 at 65 μs, after which it decreases to less than 10 W/cm^2 with t > 170 μs. The target current density and voltage are, to a first approximation, related through the expression $J_T(t) = \frac{C}{A}\frac{dV_T(t)}{dt}$ in which C is the size of capacitor bank and A is the target area. Thus, the higher rate of initial voltage drop during Ti-HIPIMS, compared to Si-HIPIMS, is associated with the higher current density (a factor of three larger).

IEDFs for (a) singly- and (b) doubly-charged Ti and Si ions produced during HIPIMS discharges operated with E_p = 10 J are shown in Fig. 2. The Ti^+ intensity reaches a maximum $I_{Ti^+,max}$ = 1.1×10^7 cps at ~5 eV, then decreases rapidly to 1.5×10^6 cps at 8 eV, and more slowly at higher energies to 8.8×10^4 cps (0.008×$I_{Ti^+,max}$) at 30 eV. In contrast, $I_{Si^+,max}$ = 1.1×10^7 cps at ~3.5 eV and I_{Si^+} decreases rapidly to 1.1×10^4 cps, < 0.001×$I_{Si^+,max}$, at 20 eV.

In order to explain the higher energy tails ($E_i > 30$ eV) in Ti IEDFs, which are not observed in Si IEDFs, we carried out time-resolved measurements which show that the presence of the high-energy tails is due to ions produced during the most energetic phase of the discharge characterized by the highest target current densities. Thus, the larger Ti high-energy tails are due to a combination of the higher peak Ti target current (1.1 A/cm^2 for Ti vs. 0.4 A/cm^2 for Si) resulting in higher plasma density in front of the Ti target (hence higher electron-impact ionization probability), and the higher mass of Ti (m_{Ti} = 47.88 amu *vs.* m_{Si} = 28.09 amu) leading to longer residence times, for a given ion energy, in the dense plasma region.

The average energy of Ti^+ ions $\langle E \rangle_{Ti^+}$ is 6.8 eV, while $\langle E \rangle_{Si^+}$ = 3.8 eV. The shape of the Ti^{2+} IEDF is similar to that of Ti^+, but with a flatter maximum shifted to a higher energy, ~7-9 eV, at which $I_{Ti^{2+},max}$ = 2.0×10^6 cps; thus $I_{Ti^{2+},max}/I_{Ti^+,max}$ = 18%. The Si^{2+} IEDF also exhibits a flatter maximum, at 6-7 eV, but with a much lower maximum intensity, $I_{Si^{2+},max}$ = 2.8×10^5 cps ($I_{Si^{2+},max}/I_{Si^+,max}$ = 2.5%).

The average energies of doubly-ionized ions are $\langle E \rangle_{Ti^{2+}}$ = 9.5 eV and $\langle E \rangle_{Si^{2+}}$ = 7.0 eV. The integrated areas ξ_{Ti^+} and $\xi_{Ti^{2+}}$ under the $I_{Ti^+}(E_i)$ and $I_{Ti^{2+}}(E_i)$ curves, $\xi_{Ti^{n+}} = \int_{E_i=1}^{E_i=E_i'} I_{Ti^{n+}}(E_i)dE_i$, correspond to the total flux of Ti^{n+} ions with $E_i \leq E_i'$ = 30 eV. From Fig. 2, ξ_{Ti^+} = 5.5×10^7 cps, $\xi_{Ti^{2+}}$ = 1.6×10^7 cps, and $\xi_{Ti^{2+}}/\xi_{Ti^+}$ = 0.29. Equivalent results for Si ions are ξ_{Si^+} = 4.1×10^7 cps and $\xi_{Si^{2+}}$= 2.2×10^6 cps, with $\xi_{Si^{2+}}/\xi_{Si^+}$ = 0.05. Lower Si^{n+} ion fluxes as a function of ion energy, especially for doubly-ionized species, are the result of the higher ionization potentials *IP* of Si (IP_{Si}^1 = 8.14 eV, IP_{Si}^2 = 16.34 eV) *vs.* Ti (IP_{Ti}^1 = 6.83 eV, IP_{Ti}^2 = 13.58 eV) compared to the ionization potentials of the sputtering gas as discussed in Section 5.

4.2. $Ti_{1-x}Si_xN_y$ film compositions

Figure 3 is a plot of $Ti_{1-x}Si_xN_y$ film compositions, *y vs. x*, for Ti-HIPIMS/Si-DCMS and Si-HIPIMS/Ti-DCMS layers. TiN_y films, grown in the absence of Si flux, are essentially stoichiometric for both sets of experiments. However, y increases approximately linearly, from 0.99 for $x = 0$ to 1.11 with $x = 0.26$, for Ti-HIPIMS/Si-DCMS films, as would be expected for two-phase TiN + Si_3N_4 mixtures, while remaining approximately constant at $y \sim 0.96$, slightly N deficient, as x is increased from 0 to 0.24 in Si-HIPIMS/Ti-DCMS films. The latter behavior is consistent with Si-HIPIMS/Ti-DCMS layers being solid-solution alloys in the NaCl phase (see XRD and TEM results below).

Trapped Ar concentrations C_{Ar} in $Ti_{1-x}Si_xN$ films are plotted in Figure 4 as a function of x. C_{Ar} is below the ERDA detection limit (0.05 at%) for Ti-HIPIMS/Si-DCMS $Ti_{1-x}Si_xN$ layers with $0 \leq x \leq 0.06$, then increases to 0.2 at% with $x = 0.13$ and 0.3 at% with $0.18 \leq x \leq 0.26$. In distinct contrast, C_{Ar} remains below detection limits for all Si-HIPIMS/Ti-DCMS $Ti_{1-x}Si_xN$ layers over the entire range in x, 0 to 0.24.

4.3. $Ti_{1-x}Si_xN$ film nanostructure

The only $Ti_{1-x}Si_xN$ XRD θ-2θ peaks observed over the 2θ range from 10 to 90° are the NaCl-structure 111 and 002 reflections. Thus, we focus on the 2θ range 30 to 50°. Figure 5 shows portions of typical θ-2θ scans as a function of the sample tilt angle ψ varied from 0 to 75° in steps of 5°. ψ is defined as the angle between the sample surface normal and the diffraction plane containing the incoming and diffracted x-ray beams. Results are presented for Ti-HIPIMS/Si-DCMS and Si-HIPIMS/Ti-DCMS $Ti_{1-x}Si_xN_y$ layers with similar Si contents, $x = 0.25 \pm 0.01$, which are also chosen for detailed TEM studies (see below). The Ti-HIPIMS/Si-DCMS $Ti_{0.74}Si_{0.26}N$ sample exhibits complete 002 out-of-plane preferred orientation (PO). 111 and 002 XRD peak

positions move to higher 2θ angles with increasing ψ, indicative of high compressive residual stresses (see Sec. 4.6). The 111 peak position obtained at the strain-free tilt angle $\psi^* = 40°$ (Ref. 47), is 36.41°, i.e., slightly lower than that of bulk TiN[63] and corresponding to a relaxed lattice parameter a_o of 4.270 Å. In contrast, Si-HIPIMS/Ti-DCMS $Ti_{0.76}Si_{0.24}N$ films are 111-oriented, with peak positions essentially independent of the tilt angle ψ and shifted toward higher 2θ angles with respect to reference TiN powder patterns.[63] The 002 peak position obtained at ψ^* is 43.06°, which corresponds to $a_o = 4.198$ Å.

Figure 6 presents plots of the relaxed lattice parameters $a_o(x)$ determined from the positions of NaCl structure 111 and/or 002 reflections acquired at the strain-free tilt angle,[47] $\psi^* = 40°$, of Ti-HIPIMS/Si-DCMS and Si-HIPIMS/Ti-DCMS $Ti_{1-x}Si_xN$ films which exhibit sufficiently high XRD peak intensities to provide reliable results. In both sample sets, the lattice parameter of pure TiN layers is 4.249±0.004 Å, in agreement with TiN powder diffraction data.[63] a_o for Ti-HIPIMS/Si-DCMS layers increases to 4.265 Å with $x = 0.04$ and remains essentially constant over the composition range $0.04 \leq x \leq 0.26$. The set of results is consistent with Si coming out of solution to form a disordered SiN_z phase in agreement with XTEM results discussed below.

A very different behavior is observed for Si-HIPIMS/Ti-DCMS $Ti_{1-x}Si_xN$ films. $a_o(x)$ decreases monotonically with increasing x content (open symbols in Fig. 6), from 4.247 Å for TiN to 4.236, 4.229, 4.218, and 4.198 Å for $Ti_{1-x}Si_xN$ with $x = 0.03$, 0.07, 0.13, and 0.24. The slope da_o/dx = -0.20 Å/mol% is in good agreement with that obtained from DFT simulations of $Ti_{1-x}Si_xN$ solid solutions, da_o/dx = -0.18 Å/mol%, in which Si and Ti are randomly distributed on the cation sublattice of the NaCl-structure. The DFT lattice parameters values are slightly larger than the experimental values at all compositions as expected since GGA, used

to approximate electron-exchange correlation effects, is known to overestimate a_o for TiN and related compounds.[64] Defect-energy calculations for the incorporation of dilute Si concentrations in TiN show a strong preference for Si to substitute for Ti on the cation sublattice rather than for N on the anion sublattice. The corresponding energies for 0.5 at% Si are 3.15 eV for Si_{Ti} and 6.19 eV for Si_N, obtained using hcp-Ti, N_2, and diamond-structure Si as reference energies to calculate chemical potentials. The Si preference for cation substitution is different than the case for TiC in which Si was shown to prefer anion sublattice substitution.[65]

Ti-HIPIMS/Si-DCMS and Si-HIPIMS/Ti-DCMS $Ti_{1-x}Si_xN$ films also differ markedly in preferred orientation as shown in Figure 7, a plot of 111 texture $T_{111} = I_{111}/(I_{111} + I_{002})$ as a function of x. Individual I_{hkl} intensities are normalized to powder diffraction data for randomly-oriented TiN.[63] Ti-HIPIMS/Si-DCMS films exhibit a strong 002 preferred orientation, with T_{111} decreasing from 0.21 with $x = 0$ to 0.03 with $x = 0.04$ to approximately zero over the composition range $0.06 \leq x \leq 0.26$. In contrast, $Ti_{1-x}Si_xN_y$ layers grown using Si-HIPIMS/Ti-DCMS display a strong 111 texture which is essentially constant with x, $T_{111} = 0.97 \pm 0.02$.

Typical cross-sectional TEM and plan-view STEM micrographs, together with selected-area electron diffraction (SAED) patterns and EDX elemental maps, of Ti-HIPIMS/Si-DCMS and Si-HIPIMS/Ti-DCMS $Ti_{1-x}Si_xN$ films with $x = 0.25 \pm 0.01$ are shown in Figures 8 and 9, respectively. The bright-field XTEM image of the $x = 0.26$ Ti-HIPIMS/Si-DCMS sample, Fig. 8(a), reveals a fine columnar structure, with an average column diameter d, obtained from the corresponding plan-view STEM image in Fig. 8(b), of ~5 nm. The relative intensities of the 111, 002, and 022 diffraction rings in the SAED patterns (Fig. 8(a) insert) show strong 002 texture, consistent with XRD results (Figs. 5 and 7). Fig. 8(c) is a plan-view elemental EDX/STEM map of the spatial distribution of Ti (red), Si (green), and N (blue). The EDX map,

acquired from the area outlined in Fig. 8(b) located in the upper part of the film, reveals SiN_z-rich layers encapsulating TiN-rich columns in agreement with earlier reports for $Ti_{1-x}Si_xN$ films with lower Si concentrations, $0.05 \leq x \leq 0.14$, grown by cathodic-arc evaporation.[35]

The bright-field XTEM image of the Si-HIPIMS/Ti-DCMS $x = 0.24$ sample, Fig. 9(a), shows a fully-dense columnar nanostructure with $d = 30\pm20$ nm. The SAED pattern in the insert displays strong 111 texture as observed by XRD (Figs. 5 and 7). Cross-sectional EDX elemental distribution maps such as those in Figs. 9(c)-9(f), together with a lattice-resolution STEM image, Fig. 9(b), reveal no indication, even at the nm scale, of a SiN_z tissue. The insert in Fig. 9(b) is an HR-STEM image, obtained along the 110 zone axis, of a single NaCl-structure column. Fig. 9(g) is a collage consisting of Ti and Si elemental EDX maps superimposed onto the lattice-resolution STEM image of Fig. 9(b). The collage provides clear evidence that the $Ti_{0.76}Si_{0.24}N$ film is single phase NaCl-structure with local sub-nm scale Si-rich and Ti-rich regions. This is in stark contrast to Ti-HIPIMS/Si-DCMS nanocomposite films with essentially the same composition (e.g., Fig. 8(b)-8(c)) which are clearly two-phase.

4.4. $Ti_{1-x}Si_xN$ valence-band spectra

XPS valence-band (VB) spectra from $x = 0.26$ Ti-HIPIMS/Si-DCMS and $x = 0.24$ Si-HIPIMS/Ti-DCMS $Ti_{1-x}Si_xN$ films are shown in Figure 10 together with Ti-HIPIMS TiN reference spectra. For the TiSiN layers, the binding-energy (BE) region between 5 and 7 eV is dominated by contributions from hybridized N 2p, Ti 3p, and Ti 3d orbitals; features at BEs less than 2 eV are primarily due to delocalized Ti 3d states.[66] The Ti-HIPIMS/Si-DCMS $Ti_{0.74}Si_{0.26}N$ spectrum in the VB region exhibits a density-of-states (DOS) distribution across the Fermi level E_f that is significantly lower than that of the TiN reference sample. Since the

DOS at E_f is due to delocalized states responsible for electrical conductivity, this result is consistent with the very small TiN crystallite size due to phase segregation (see XTEM/TEM results above) which leads to increased grain boundary scattering and, hence, decreased conductivity. DOS at E_f is further lowered due to the absence of a contribution from the considerable volume fraction of SiN_z tissue phase which, as shown in Sec. 4.2, has a stoichiometry close to Si_3N_4. In contrast, the DOS at E_f for single-phase NaCl-structure Si-HIPIMS/Ti-DCMS $Ti_{0.76}Si_{0.24}N$ layers is essentially the same as that of the reference TiN layer.

4.5. $Ti_{1-x}Si_xN$ nanoindentation hardness and elastic modulus

Fig.11 shows the hardness H of $Ti_{1-x}Si_xN$ films as a function of x for both sample sets. TiN films grown by Ti-HIPIMS/Si-DCMS have a hardness of 26.9 GPa which increases rapidly to 39.4±0.4, 45.0±1.2, and 40.9±1.5 GPa for $Ti_{1-x}Si_xN_y$ layers with $0.04 \leq x \leq 0.06$, 0.13, and $0.18 \leq x \leq 0.26$, respectively. For Si-HIPIMS/Ti-DCMS films, H decreases from 20.8 GPa with $x = 0$ to 14.1 GPa for $x = 0.03$ and remains approximately constant at 13.6±0.9 GPa with $0.07 \leq x \leq 0.24$. Thus, $H(x)$ exhibits an inverse behavior for Ti-HIPIMS/Si-DCMS compared to Si-HIPIMS/Ti-DCMS.

Results for $Ti_{1-x}Si_xN$ elastic moduli $E(x)$, plotted in Figure 12, exhibit general behavior similar to that of $H(x)$. For Ti-HIPIMS/Si-DCMS films, elastic moduli increase from $E = 457$ GPa with $x = 0$ to 499±18 GPa with $0.04 \leq x \leq 0.26$. In the case of Si-HIPIMS/Ti-DCMS $Ti_{1-x}Si_xN$ layers, $E(x)$ is initially higher than for Ti-HIPIMS/Si-DCMS with $E(x{=}0) = 487$ GPa; however, it decreases rapidly with increasing x to 395, 386, 360, and 354 GPa with $x = 0.03$, 0.07, 0.13, and 0.24.

Elastic moduli values obtained from DFT simulations $E_{DFT}(x)$ for $Ti_{1-x}Si_xN$ solid solutions with $0 < x \leq 0.25$, are in qualitative agreement with experimental results for Si-

HIPIMS/Ti-DCMS alloys. E_{DFT} = 463 GPa with x = 0.05 and decreases slowly to 444, 416, and 393 GPa with x = 0.11, 0.17, and 0.25.

4.6. $Ti_{1-x}Si_xN$ residual stress

Residual stress values σ for Ti-HIPIMS/Si-DCMS and Si-HIPIMS/Ti-DCMS $Ti_{1-x}Si_xN$ layers are plotted as a function of x in Figure 13. For Ti-HIPIMS/Si-DCMS films, σ increases rapidly from -1.5 GPa for TiN to -2.6, -4.5, and -6.7 GPa for $Ti_{1-x}Si_xN$ layers with x = 0.04, 0.06, and 0.13, to saturate at -8.0±0.4 GPa for $0.18 \leq x \leq 0.26$. In contrast, all Si-HIPIMS/Ti-DCMS films, $0 \leq x \leq 0.24$, are nearly stress-free with σ = 0.5±0.3 GPa.

5. Discussion

The results show that switching the HIPIMS and DCMS power supplies between the Ti and Si targets to grow $Ti_{1-x}Si_xN_y$ films by Ti-HIPIMS/Si-DCMS and Si-HIPIMS/Ti-DCMS has a decisive influence on the nanostructure, nanochemistry, and macroscopic properties of as-deposited layers. XTEM and plan view TEM images combined with EDX compositional maps (Fig. 8) reveal that Ti-HIPIMS/Si-DCMS films with x = 0.26 are columnar nanocomposites consisting of elongated TiN-rich crystallites, each encapsulated by a thin SiN_z tissue phase. Average column widths are ~5 nm. XRD scans and SAED patterns reveal that the nanocolumns have very strong 002 texture. The tissue phase is likely crystalline for the first one or two monolayers,[25] beyond which it is disordered as indicated by the lack of additional diffraction rings in SAED patterns. The Ti-HIPIMS/Si-DCMS $Ti_{1-x}Si_xN_y$ compositional results presented in Fig. 3 show that y increases continuously with increasing x, as would be expected for two-phase TiN + Si_3N_4 mixtures, consistent with electron microscopy observations. The relaxed

lattice parameter of TiN-rich crystallites remains constant throughout the entire compositional range, $0.04 \leq x \leq 0.26$.

In contrast, Si-HIPIMS/Ti-DCMS films are solid-solution $Ti_{1-x}Si_xN_y$ pseudobinary alloys with $x \leq 0.24$, the highest SiN concentration yet reported. XRD scans, XTEM images, and SAED patterns demonstrate that the films are fully-dense with a single-phase NaCl crystal structure consisting of columns with an average width of 30±20 nm and a strong 111 texture. Cross-sectional HR-TEM and EDX elemental maps of $Ti_{0.76}Si_{0.24}N$ (Fig. 9) reveal uniform elemental distribution, at the nm scale, of Ti, Si, and N. Independent evidence for solid solution formation derives from analyses of Si-HIPIMS/Ti-DCMS $Ti_{1-x}Si_xN_y$ film composition y vs. x (Fig. 3), relaxed lattice parameters $a_o(x)$ (Fig. 6), and XPS valence band spectra (Fig. 10). Increasing the SiN concentration has no effect on the overall N/(Ti + Si) ratio, which remains constant as a function of x as Si substitutes for Ti on the cation sublattice. In addition, $a_o(x)$ decreases monotonically with increasing x (Fig. 6) due to the smaller size of Si than Ti atoms, with a slope da_o/dx = -0.20 Å/mol% in good agreement with DFT calculations for random $Ti_{1-x}Si_xN$ solid solutions. Finally, the electron density-of-states at the Fermi level (Fig. 10), due primarily to delocalized Ti 3d states, is essentially the same for Si-HIPIMS/Ti-DCMS $Ti_{0.76}Si_{0.24}N$ and the reference TiN layer. This is in sharp contrast to XPS results for phase-separated Ti-HIPIMS/Si-DCMS $Ti_{0.74}Si_{0.26}N$ (Fig. 10), for which the small size of TiN-rich crystallites and the presence of a disordered SiN_z tissue phase, with composition close to that of semiconducting Si_3N_4, limits the extent of electron delocalization and lowers the total DOS at E_f.

Ion irradiation of growing films has been shown to play a crucial and deterministic role in controlling film nanostructure.[1,2,3] During sputter deposition in the hybrid HIPIMS/DCMS

configuration, the film growth surface is subject to an intense metal-ion flux during the short HIPIMS pulses (see Fig. 2) and a continuous flux of very low-energy, 10 eV, gas ions (Ar^+, N_2^+, and N^+) ions[67] during the dc phase. Thus, co-sputtering in a hybrid configuration in which one target is operated in HIPIMS, while the other is operated in DCMS mode, presents the opportunity to selectively probe the effect of individual energetic metal ion fluxes on the evolution of film nanostructure and physical properties. The total metal deposition between HIPIMS pulses is a small fraction of a monolayer (< 2×10^{-3} ML); thus, newly-deposited film atoms are exposed to intense incident metal-ion irradiation during the subsequent HIPIMS pulse.

Our previous results for hybrid HIPIMS/DCMS growth of metastable cubic $Ti_{1-x}Al_xN$ alloys revealed a large asymmetry between the effects of energetic Al^{n+} and Ti^{n+} (n = 1, 2) ion irradiation on the evolution of film nanostructure and phase content.[16,17,20,21] $Ti_{1-x}Al_xN$ is known to be very sensitive to ion-irradiation-induced phase separation. We showed that the average metal-ion momentum $\langle p_d \rangle$ per deposited atom controls both the phase composition and stress evolution.[20,21] With $\langle p_d \rangle > \langle p_d^* \rangle \simeq 135$ [eV-amu]$^{1/2}$, as-deposited $Ti_{1-x}Al_xN$ films are two-phase mixtures for all x values ≥ 0.40. $\langle p_d^* \rangle$ is easily exceeded during Ti-HIPIMS, even with no intentional bias, since the growing film is subjected to a high flux of relatively heavy (m_{Ti} = 47.88 amu) doubly-ionized Ti^{2+}. Double ionization results from the fact that the second ionization potential IP_{Ti}^2 of Ti is lower than the first ionization potential IP_{Ar}^1 of Ar. In contrast, Al^{2+} ion flux is insignificant during Al-HIPIMS since $IP_{Al}^2 > IP_{Ar}^1$. Thus, the relatively low mass (m_{Al} = 26.98 amu) and single charge of the Al^+ ion flux permits tuning properties of metastable cubic $Ti_{0.38}Al_{0.62}N$ by adjusting the incident Al^+ ion energy to obtain single-phase alloys with

metastable cubic AlN concentrations up to x_{max} ~ 0.65. The alloys exhibit high hardness, H > 30 GPa, with low residual stress, σ = -0.2 GPa.

The present experiments are carried out under comparable conditions of N_2/Ar gas composition, total pressure, film growth temperature, and substrate bias. Similar to the TiAlN case,[16] ion mass spectrometry results (Fig. 2) reveal a large asymmetry between metal-ion fluxes incident at the growing film surface during Ti-HIPIMS/Si-DCMS compared to Si-HIPIMS/Ti-DCMS. Metal-ion IEDF's differ substantially for the two cases due to the ionization potentials IP of Si (IP_{Si}^1 = 8.14 eV, IP_{Si}^2 = 16.34 eV) being higher than those of Ti (IP_{Ti}^1 = 6.83 eV, IP_{Ti}^2 = 13.58 eV). Ti^+ IEDFs recorded during Ti-HIPIMS/Si-DCMS possess high-energy tails ($0.008\times I_{Ti^+,max}$ at 30 eV), which are not present during Si^+ Si-HIPIMS/Ti-DCMS, for which the IEDFs fall off much more rapidly ($< 0.001\times I_{Si^+,max}$ at 20 eV). There is also a dramatic difference in the doubly-ionized metal ion flux for the two target configurations. The total doubly-to-singly ionized metal ion flux ratio, $\xi_{Me^{2+}}/\xi_{Me^+}$, is 0.29 for Ti, but only 0.05 for Si. In the Ti-HIPIMS case, IP_{Ti}^2 is lower than both IP_{Ar}^1 (15.76 eV) and $IP_{N_2}^1$ (15.55 eV),[68] resulting in HIPIMS pulses with significant electron populations having energies in the range $IP_{Ti}^2 < E_e < IP_{N_2}^1$; i.e., too low to ionize gas species, yet high enough to produce doubly-ionized Ti^{2+}. For Si-HIPIMS, $IP_{Si}^2 > IP_{Ar}^1$ and gas ionization depletes the population of electrons with $E_e > IP_{Ar}^1$. Thus, the Si^{2+} creation rate is significantly lower than that of Ti^{2+}, as shown in Fig. 2(b). The total metal-ion flux, $\xi_{Me^+} + \xi_{Me^{2+}}$, integrated over 200-µs-pulses, is 1.7× higher during Ti-HIPIMS than for Si-HIPIMS.

The large asymmetry between Ti-HIPIMS/Si-DCMS and Si-HIPIMS/Ti-DCMS metal-ion flux intensities and average ion energies incident at the film growth surface results in correspondingly large differences in the average momentum transfer per deposited atom,[69]

$$\langle p_d \rangle_i = \sum_{n=1}^{N} \sqrt{2m_i\gamma_i \left(E_i^o + ne\left(V_s - V_{pl}\right)\right)} \times \xi_{i,n}/\xi_{Me}, \quad (7)$$

for which

$$\gamma_i = 4m_i m_f/\left(m_i + m_f\right)^2. \quad (8)$$

m_i is the ion mass, γ_i is the energy transfer function, E_i^o denotes the average energy of ions entering the anode sheath, n is the charge state of the ion, V_{pl} is the plasma potential (~10 V),[70] and $\xi_{i,n}$ is the flux of metal ions i with charge state n. In the present study, the highest detected metal-ion charge state n is 2 and we discard the term E_i^o in Eqn. (7), which is small compared to $e(V_s - V_{pl})$. Since the later term is similar during Ti-HIPIMS/Si-DCMS and Si-HIPIMS/Ti-DCMS, we can express the $\langle p_d \rangle_{Ti^{n+}}/\langle p_d \rangle_{Si^{n+}}$ ratio as

$$\langle p_d \rangle_{Ti^{n+}}/\langle p_d \rangle_{Si^{n+}} = \frac{\xi_{Ti^+} + \sqrt{2}\xi_{Ti^{2+}}}{\xi_{Si^+} + \sqrt{2}\xi_{Si^{2+}}} \left(\frac{\xi_{Si-HIPIMS}}{\xi_{Ti-HIPIMS}}\right) \sqrt{\frac{m_{Ti}\gamma_{Ti}}{m_{Si}\gamma_{Si}}}. \quad (9)$$

From ion mass spectroscopy analyses, $\left(\xi_{Ti^+} + \sqrt{2}\xi_{Ti^{2+}}\right)/\left(\xi_{Si^+} + \sqrt{2}\xi_{Si^{2+}}\right) = 1.8$. The second term in Eqn.(9), $\xi_{Si-HIPIMS}/\xi_{Ti-HIPIMS}$, is the ratio of the total integrated metal fluxes incident at the film growth surface during 200-µs Si- and Ti-HIPIMS pulses. $\xi_{Si-HIPIMS}$ is more than 8× larger than $\xi_{Ti-HIPIMS}$, due primarily to higher metal ionization during Ti-HIPIMS. Ar^+ sputter yields, estimated using TRIM,[50] are nearly the same for Si and Ti at the ion energies used in these experiments; thus, there is significant Ti^{n+} metal-ion transport back to the HIPIMS target (the "return effect").[43] This requires the DCMS target to be operated at correspondingly lower power levels in order to obtain films with the desired concentrations. For example, in the case of $Ti_{1-x}Si_xN$ films with $x = 0.25\pm0.01$, the film thickness deposited during one pulse in the Si-HIPIMS/Ti-DCMS configuration is 1.17×10^{-2} Å compared to 0.14×10^{-2} Å for Ti-HIPIMS/Si-DCMS. This corresponds to $\xi_{Si-HIPIMS}/\xi_{Ti-HIPIMS} = 8.4$. Therefore, accounting for

differences in metal ion mass (m_{Ti} = 47.88 amu, m_{Si} =28.09 amu), and the energy-transfer function (γ_{Ti} = 0.993, γ_{Si} = 0.885), we estimate the ratio $\langle p_d \rangle_{Ti^{n+}} / \langle p_d \rangle_{Si^{n+}}$ to be ~21 during the growth of $Ti_{1-x}Si_xN$ with x = 0.25±0.01.

Our results show that the large asymmetry between the Ti^{n+} and Si^{n+} metal ion fluxes has a dramatic effect on the evolution of $Ti_{1-x}Si_xN$ film texture (Fig. 7), hardness (Fig. 11), elastic modulus (Fig. 12), and residual stress (Fig. 13). Films grown in Ti-HIPIMS/Si-DCMS mode are superhard over a very wide compositional range, $0.04 \leq x \leq 0.26$; the maximum hardness, H = 45 GPa, is obtained with x = 0.13. They possess a mean E value of 498 GPa, are 002-oriented, and exhibit very high compressive stress, σ = -7±1 GPa. In contrast, Si-HIPIMS/Ti-DCMS films, with H ~ 14 GPa and E ~ 374 GPa over the composition range $0.03 \leq x \leq 0.24$, possess 111 preferred orientation and are essentially stress-free (σ~0.5 GPa).

The large spread in $H(x)$, $E(x)$, and $\sigma(x)$ values between Ti-HIPIMS/Si-DCMS and Si-HIPIMS/Ti-DCMS $Ti_{1-x}Si_xN$ layers is primarily due to distinctly different phase content and nanostructure (see Figs. 8 and 9) resulting from differences in the average mass, charge state, and type of metal-ion flux incident at the growth surface. A better mass match between incident Ti^+ ions (as opposed to Si^+ ions) and film constituents during Ti-HIPIMS/Si-DCMS film growth, together with higher metal-ion/metal-atom flux ratios and larger fractions of doubly-ionized species (see Fig. 2(b)) result in much higher average momentum transfer per deposited atom $\langle p_d \rangle$ during HIPIMS pulses. This leads, in turn, to enhanced adatom mean free paths giving rise to a higher probability for smaller Si atoms to segregate to column boundaries, thus resulting in a phase-separated nanocomposite structure for $Ti_{1-x}Si_xN$ films with $0.04 \leq x \leq 0.26$. $H(x)$ values presented here for Ti-HIPIMS/Si-DCMS films are similar to those reported for nanocomposites[32,33,30] for which superhardness is attributed to the combination of the TiN-rich

grains being too small for effective dislocation nucleation and glide, while the covalently-bonded tissue phase inhibits grain-boundary sliding.[25] The extremely high compressive stresses in Ti-HIPIMS/Si-DCMS layers also contribute to the measured hardness.

Intense Ti^{+}/Ti^{2+} metal ion bombardment clearly favors 002 preferred orientation (see Fig. 7), which is directly related to collision cascade effects. Grains with more open channel directions, such as 002, with the projected atom density lower by a factor of $\sqrt{3}$ than in the 111 direction, have higher survival rates, since the incident ion energy is distributed over larger depths leading to lower sputtering yields and less lattice distortion.[1] As a consequence of the 002 preferred orientation, incident Ar ions are implanted to larger depths, compared to 111-oriented layers, due to the larger open channel areas. Thus, a significant concentration of Ar remains trapped in Ti-HIPIMS/Si-DCMS $Ti_{1-x}Si_xN$ films as interstitials (see Fig. 4) and contributes to the observed high compressive stresses (Fig. 13). The nanocomposite structure, mechanical properties, and residual stress levels of layers grown in this target configuration resemble those obtained with cathodic arc deposition,[35] for which intense Ti^{n+} (n = 1, 2, 3,..) metal-ion irradiation is also present.[71]

$\langle p_d \rangle$ is ~20 times lower during Si-HIPIMS/Ti-DCMS than for Ti-HIPIMS/Si-DCMS due to the lower Si^{n+} ion mass compared to Ti^{n+}, the lower doubly-ionized fraction in the incident ion flux, and the lower ion-to-metal flux ratio. While Ti^{n+} ions transfer momentum very effectively to Ti lattice atom, the lighter Si^{+} ions penetrate the film and become incorporated in cation sublattice positions preserving the metastable NaCl-structure. As a result, we obtain TiSiN solid solutions with the highest compositional range, up to $x = 0.24$, yet reported. Low H and E values for Si-HIPIMS/Ti-DCMS $Ti_{1-x}Si_xN$ alloys with $0.03 \leq x \leq 0.24$

are consistent with DFT simulation results for TiSiN solid solutions, in which Si and Ti atoms are randomly distributed on the NaCl-structure cation sublattice.

6. Conclusions

We use a hybrid HIPIMS/DCMS two-target co-sputtering configuration, in which one target (either Ti or Si) is powered by HIPIMS while the other is powered by DCMS, for growth of $Ti_{1-x}Si_xN$ films with compositions $0 \leq x \leq 0.26$. Markedly different film growth pathways are obtained depending upon which target is powered by HIPIMS with, in both cases, a substrate bias applied in synchronous with the HIPIMS pulse. The observed divergence in film nanostructure, phase content, and mechanical properties between layers grown in Ti-HIPIMS/Si-DCMS and Si-HIPIMS/Ti-DCMS configuration is due to distinctly different metal-ion irradiation conditions, Ti^+/Ti^{2+} *vs*. Si^+/Si^{2+}, during film growth.

Ti-HIPIMS/Si-DCMS films with $x = 0.26$ are columnar nanocomposites consisting of elongated 002-oriented TiN-rich crystallites, with average column widths of ~5 nm, encapsulated by a thin SiN_z tissue phases. In contradistinction, Si-HIPIMS/Ti-DCMS films with $x \leq 0.24$ are NaCl-structure solid-solution $Ti_{1-x}Si_xN_y$ pseudobinary alloys with a dense columnar nanostructure, an average column width of 30±20 nm, and a strong 111 texture.

During Ti-HIPIMS/Si-DCMS, the doubly-to-singly ionized metal ion flux ratio $\xi_{Ti^{2+}}/\xi_{Ti^+}$ at the growth surface during the Ti HIPIMS pulse is high, 0.29, due to the second ionization potential of Ti (IP_{Ti}^2 = 13.58 eV) being lower than the first ionization potential of the sputtering gas (IP_{Ar}^1 = 15.76 eV). A better mass match between incident Ti^+ ions and the average film atomic mass, higher metal-ion/metal-atom ratios during HIPIMS pulses, and a high fraction of doubly-ionized species results in an average momentum transfer per deposited atom $\langle p_d \rangle$ ~20 times higher

for Ti-HIPIMS/Si-DCMS than during Si-HIPIMS/Ti-DCMS. As a consequence, adatom mean free paths are increased leading to the segregation of smaller Si atoms to column boundaries and the formation of a nanocomposite structure consisting of TiN-rich nanocolumns encapsulated in SiN_x tissue phases. Ti-HIPIMS/Si-DCMS $Ti_{1-x}Si_xN$ films are superhard over a composition range that is significantly wider than reported previously, $0.04 \leq x \leq 0.26$, with a maximum hardness, $H = 45$ GPa, for layers with $x = 0.13$. However, residual stresses are also high with an average value of -7±1 GPa.

In sharp contrast, during Si-HIPIMS/Ti-DCMS $Ti_{1-x}Si_xN$ film growth, the flux of doubly-ionized metal ions is lower, $\xi_{Si^{2+}}/\xi_{Si^{+}} = 0.05$, due to high IP_{Si}^{2} (16.34 eV) compared to IP_{Ar}^{1}. This, together with the lower mass of Si, low metal-ion/metal-atom flux ratio during HIPIMS pulses, and poorer mass match between incident Si^{+} ions average film atomic mass results in relatively low $\langle p_d \rangle$ values. As a consequence, Si is trapped in the metastable $Ti_{1-x}Si_xN$ NaCl structure to form solid solutions over the highest compositional range yet reported, $0 \leq x \leq 0.24$.

7. Acknowledgments

Financial support from the European Research Council (ERC) through an Advanced Grant #227754, the VINN Excellence Center *Functional Nanoscale Materials* (FunMat) Grant #2005-02666, the Knut and Alice Wallenberg Foundation Grant #2011.0143, the Swedish Government Strategic Faculty Grant in Materials Science to Linköping University (SFO Mat-LiU AFM), and Swedish Research Council (VR) Project Grants #2014-5790, #621-2011-4417, and 330-2014-6336 are gratefully acknowledged.

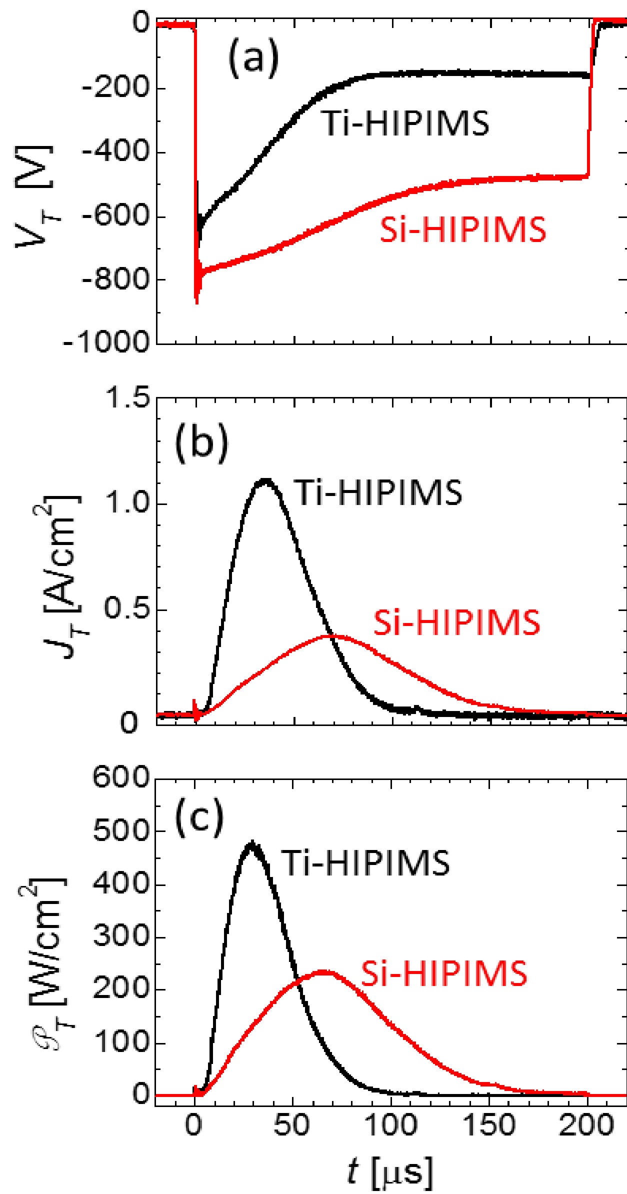

Greczynski et al fig. 1

Fig. 1. (a) Target voltage $V_T(t)$, (b) current density $J_T(t)$, and (c) power density $\mathcal{P}_T(t)$ waveforms recorded during 200 μs Ti and Si HIPIMS pulses.

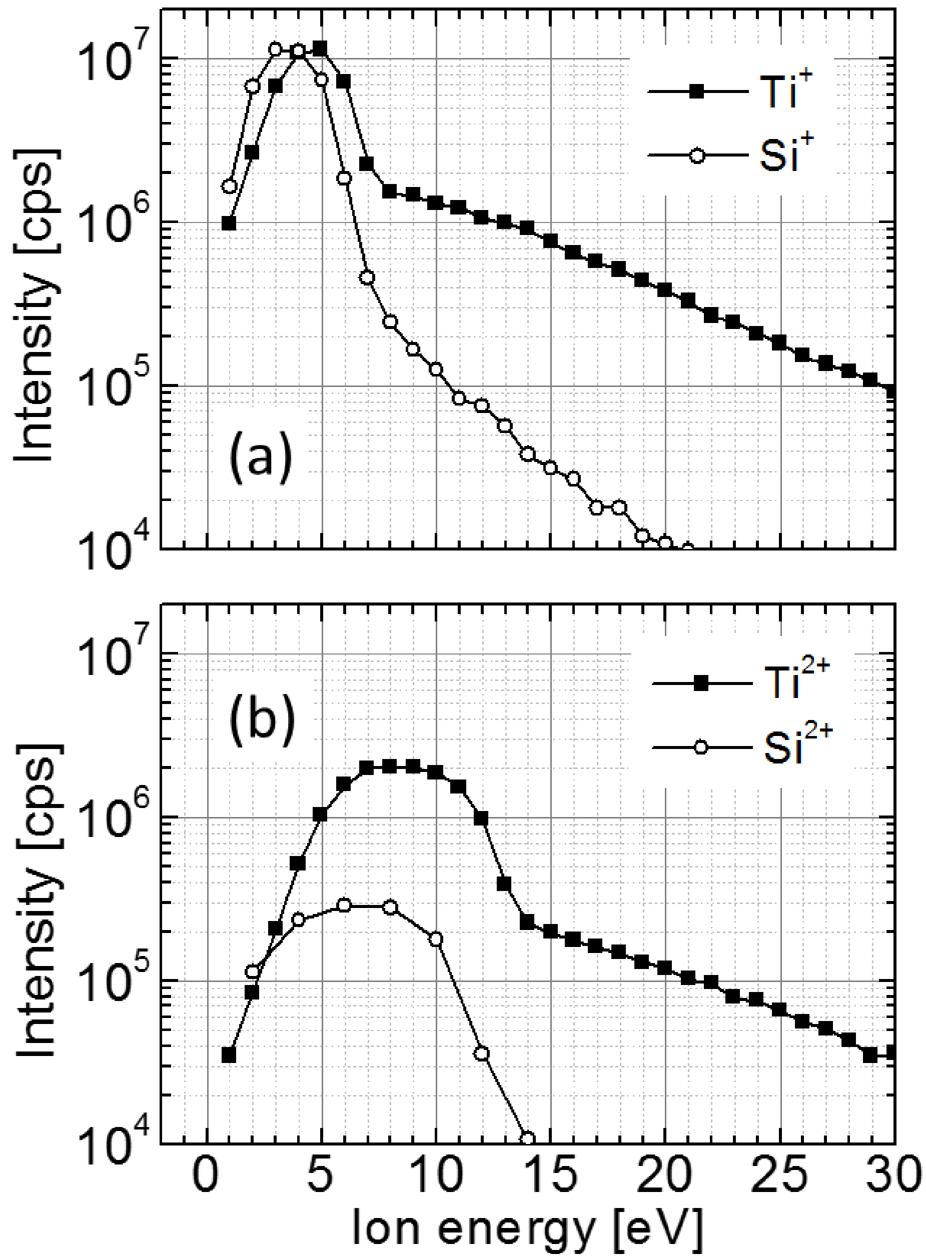

Greczynski et al fig. 2

Fig. 2. Ion intensity *vs.* energy measured at the substrate position for (a) singly-charged Ti^{+} and Si^{+} ions, and (b) doubly-charged Ti^{2+} and Si^{2+} ions during Ti-HIPIMS and Si-HIPIMS pulses.

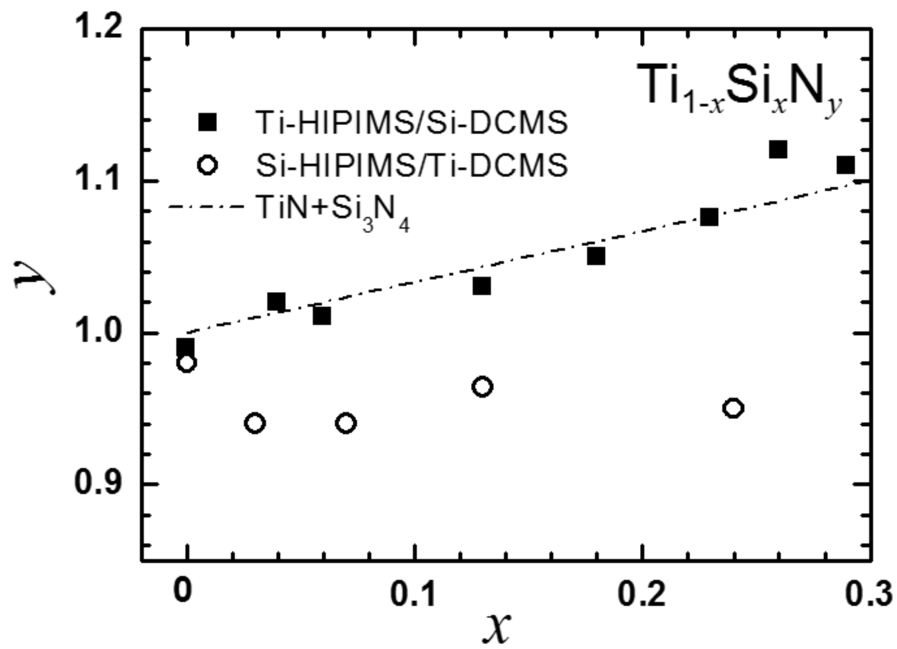

Greczynski et al fig. 3

Fig. 3. $Ti_{1-x}Si_xN_y$ film compositions, y vs. x, for Ti-HIPIMS/Si-DCMS and Si-HIPIMS/Ti-DCMS layers grown on Si(001) substrates at T_s = 500 °C.

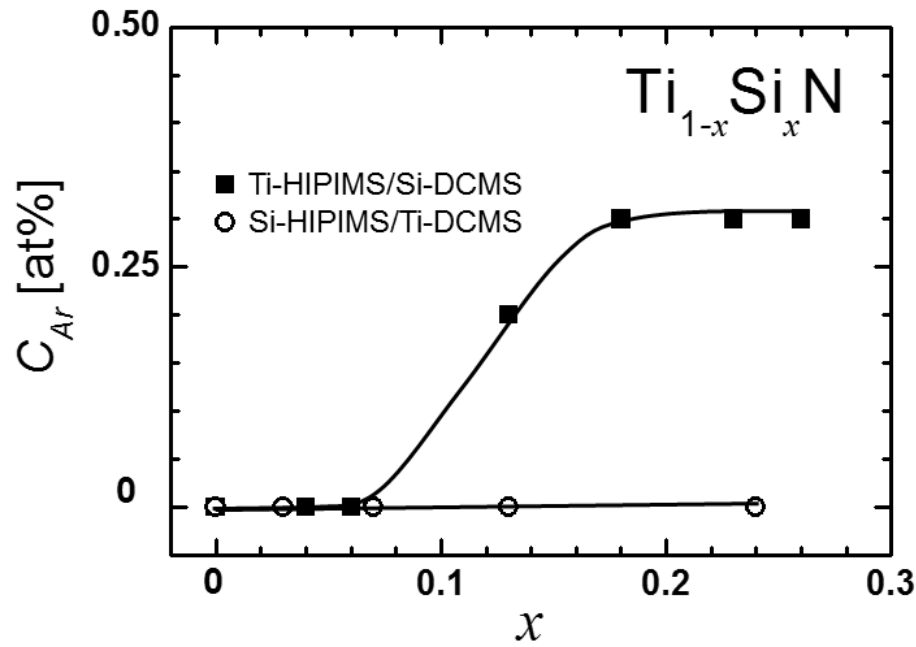

Greczynski et al fig. 4

Fig. 4. Trapped Ar concentrations C_{Ar} in $Ti_{1-x}Si_xN$ films grown on Si(001) substrates by hybrid Ti-HIPIMS/Si-DCMS and Si-HIPIMS/Ti-DCMS co-sputter deposition at T_s = 500 °C.

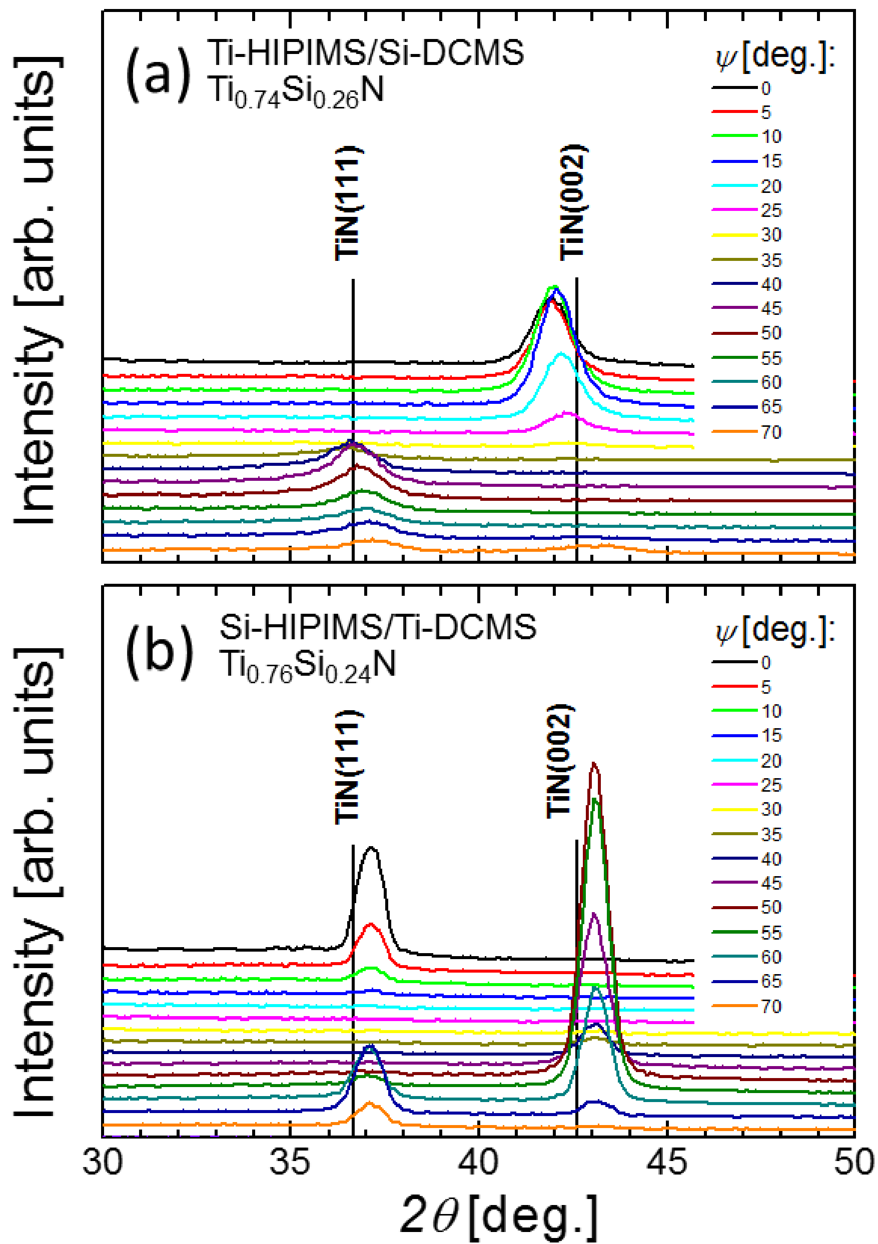

Greczynski et al fig. 5

Fig. 5. XRD θ-2θ scans as a function of the tilt angle ψ for (a) Ti-HIPIMS/Si-DCMS and (b) Si-HIPIMS/Ti-DCMS $Ti_{1-x}Si_xN$ layers, with Si contents x = 0.25±0.01, grown on Si(001) substrates at T_s = 500 °C.

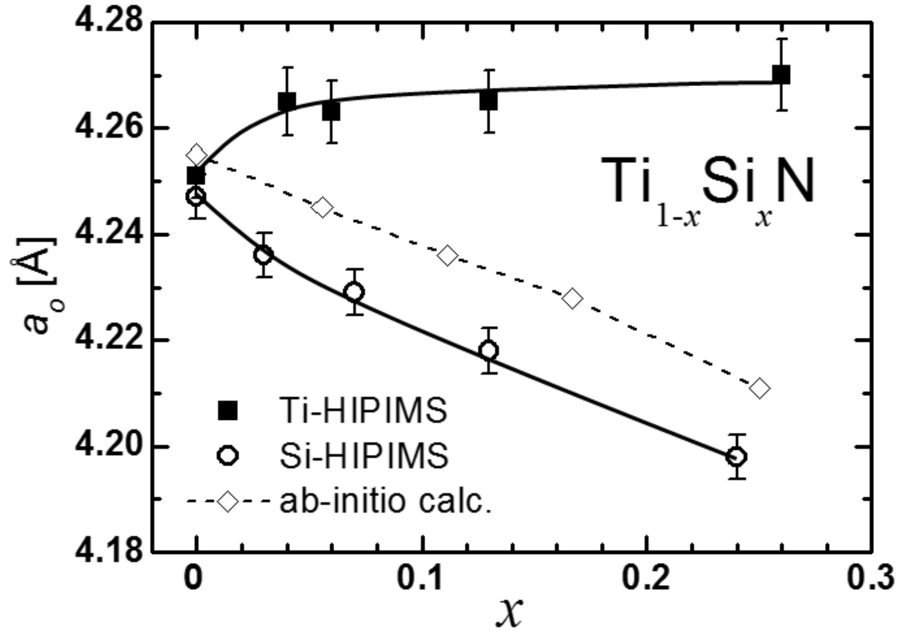

Greczynski et al fig. 6

Fig. 6. Relaxed lattice parameters $a_o(x)$, determined from XRD θ-2θ scans at the strain-free tilt angle ψ^*,[16] of Ti-HIPIMS/Si-DCMS and Si-HIPIMS/Ti-DCMS $Ti_{1-x}Si_xN$ films grown on Si(001) substrates at T_s = 500 °C. The open diamond shaped data points are obtained from first-principles calculations based upon $Ti_{1-x}Si_xN$ random alloys.

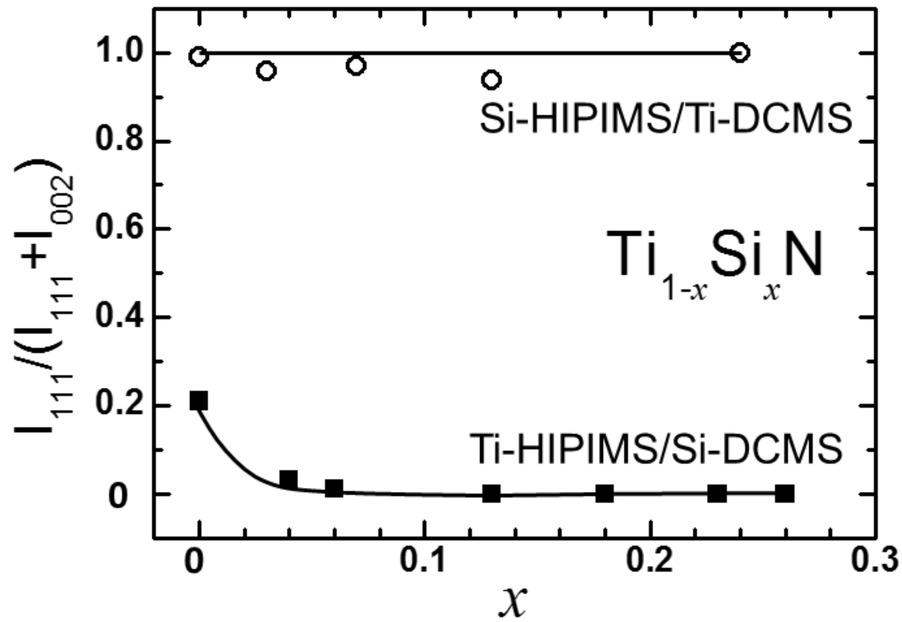

Greczynski et al fig. 7

Fig. 7. XRD 111 texture ratios $T_{111} = I_{111}/(I_{111} + I_{002})$ as a function of x for Ti-HIPIMS/Si-DCMS and Si-HIPIMS/Ti-DCMS $Ti_{1-x}Si_xN$ films grown on Si(001) substrates at T_s = 500 °C. All I_{hkl} intensities are normalized to powder diffraction data for randomly-oriented TiN.

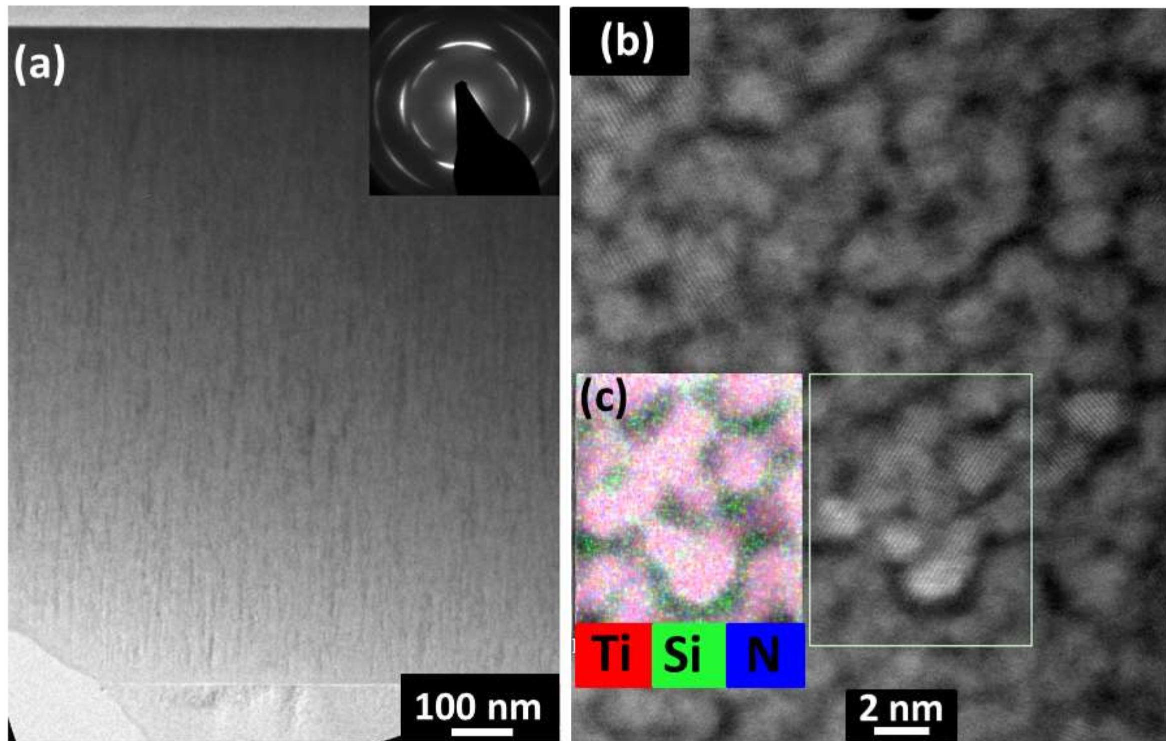

Greczynski et al fig. 8

Fig. 8. (a) Bright-field XTEM image, with a corresponding SAED pattern, of a $Ti_{0.74}Si_{0.26}N$ Ti-HIPIMS/Si-DCMS film grown on Si(001) substrate at T_s = 500 °C. (b) Plan-view STEM micrograph, and (c) plan-view EDX/STEM elemental maps, showing Ti (red), Si (green), and N (blue) spatial distributions, acquired from the area outlined in panel (b).

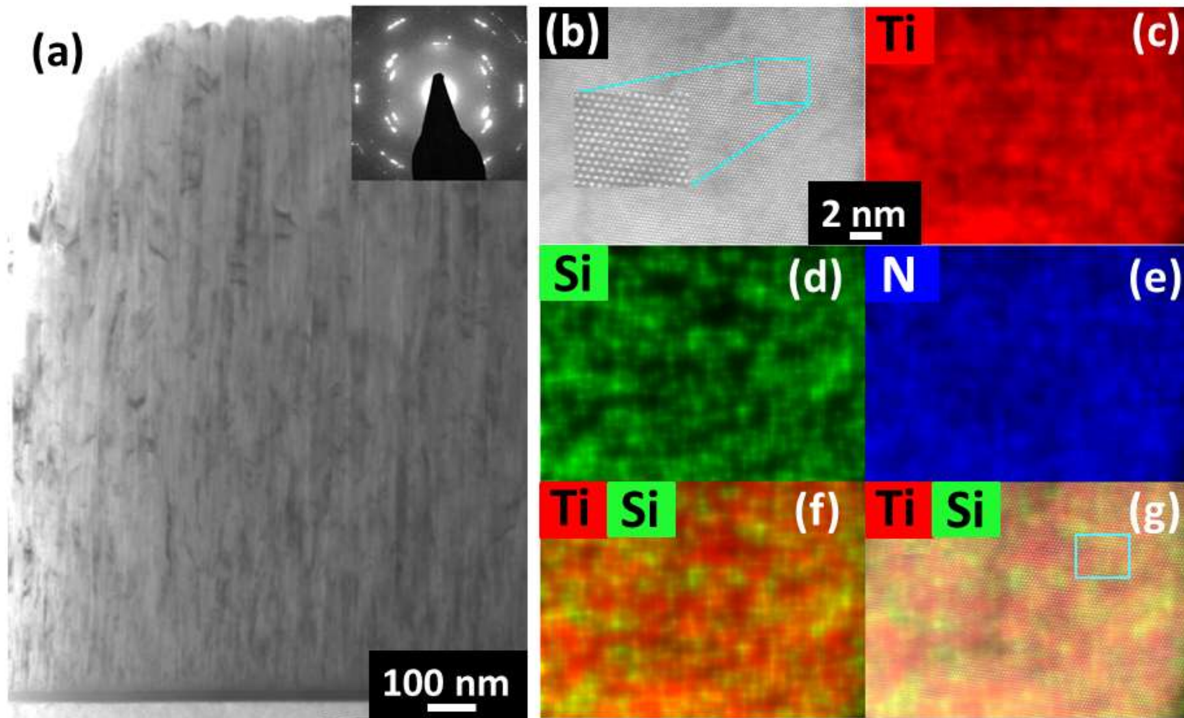

Greczynski et al fig. 9

Fig. 9. (a) Bright-field XTEM image, with a corresponding SAED pattern, of a $Ti_{0.76}Si_{0.24}N$ Si-HIPIMS/Ti-DCMS film grown on Si(001) substrate at T_s = 500 °C. (b) Cross-sectional STEM micrograph, including an HRSTEM lattice-resolved image, (c)-(f) cross-sectional EDX elemental maps showing Ti (red), Si (green), and N (blue) spatial distributions, and (g) Ti and Si elemental EDX maps together with the lattice-resolved STEM image.

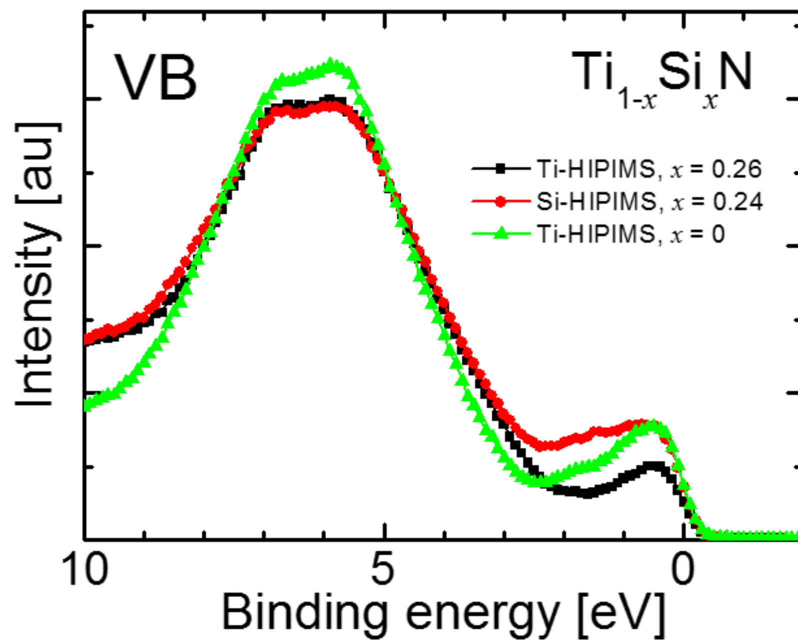

Greczynski et al fig. 10

Fig. 10. XPS valence-band spectra from Ti-HIPIMS/Si-DCMS (x = 0.26), Si-HIPIMS/Ti-DCMS (x = 0.24) $Ti_{1-x}Si_xN$ films, and Ti-HIPIMS TiN reference films grown on Si(001) substrates at T_s = 500 °C.

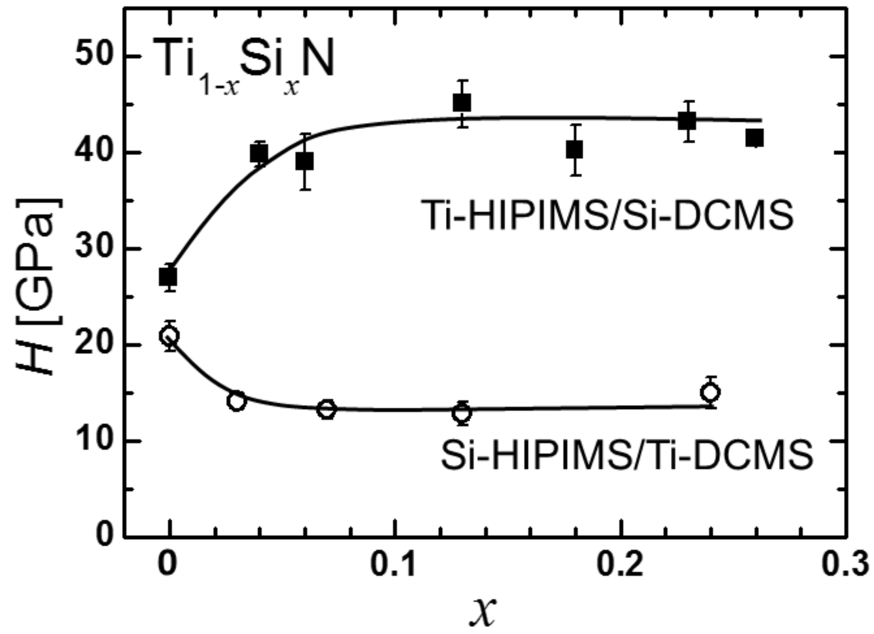

Greczynski et al fig. 11

Fig. 11. Nanoindentation hardnesses *H(x)* of Ti-HIPIMS/Si-DCMS and Si-HIPIMS/Ti-DCMS $Ti_{1-x}Si_xN$ films grown on Si(001) substrates at T_s = 500 °C.

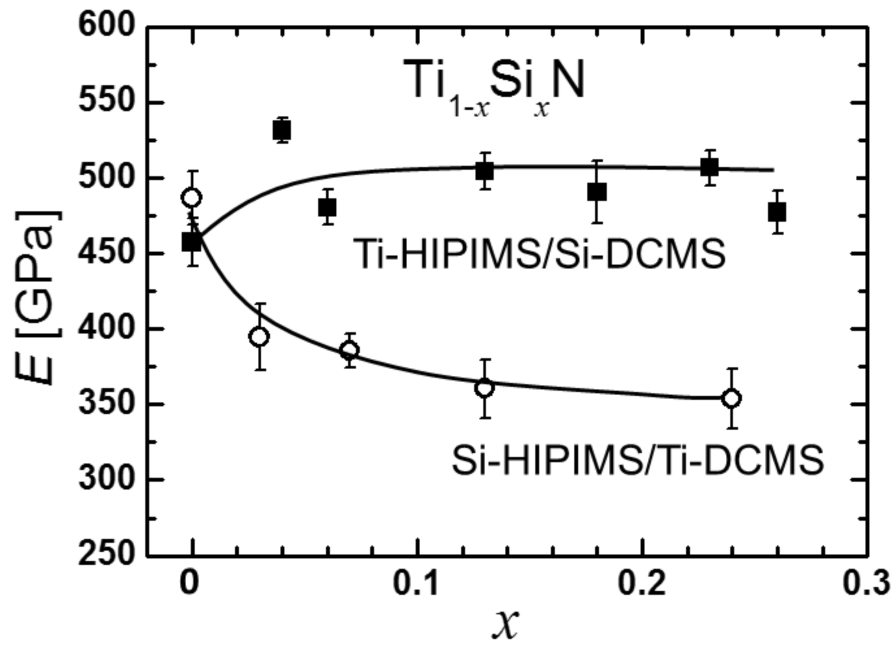

Greczynski et al fig. 12

Fig. 12. Nanoindentation elastic moduli *E(x)* of Ti-HIPIMS/Si-DCMS and Si-HIPIMS/Ti-DCMS $Ti_{1-x}Si_xN$ films grown on Si(001) substrates at T_s = 500 °C.

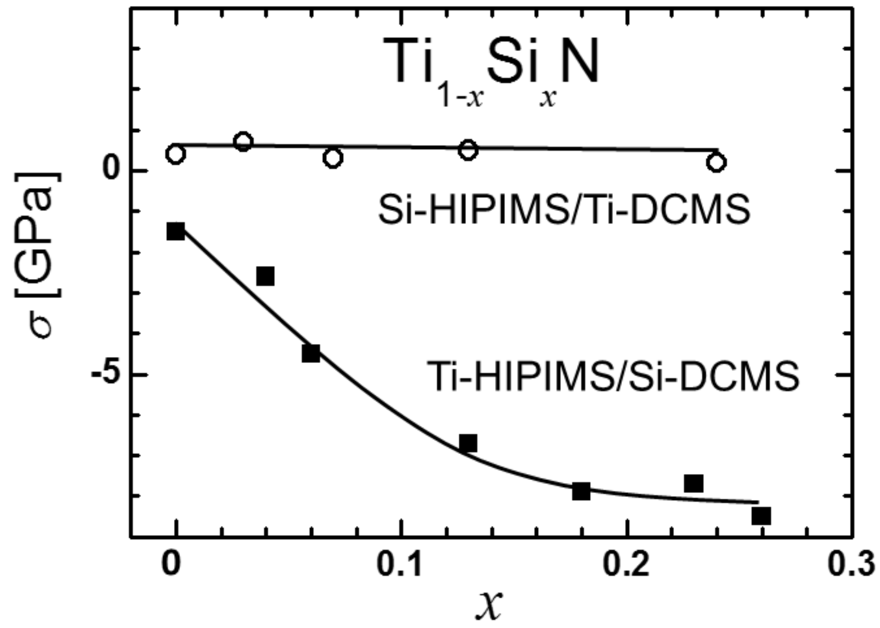

Greczynski et al fig. 13

Fig. 13. Residual stress $\sigma(x)$ of Ti-HIPIMS/Si-DCMS and Si-HIPIMS/Ti-DCMS $Ti_{1-x}Si_xN$ films grown on Si(001) substrates at $T_s = 500$ °C.

References:

[1] I. Petrov, P.B. Barna, L. Hultman, J.E. Greene *J. Vac. Sci. Technol. A* 21 (2003) 117

[2] M.A. Hasan, S.A. Barnett, J.-E. Sundgren, J.E. Greene, *J. Vac. Sci. Technol. A* 5 (1987) 1883.

[3] Y.-W. Kim, I. Petrov, H. Ito, and J. E. Greene, *J. Vac. Sci. Technol. A* 13 (1995) 2836.

[4] Y.-W. Kim, I. Petrov, J. E. Greene and S. M. Rossnagel, *J. Vac. Sci. Technol. A* 14 (1996) 346.

[5] I. Petrov, L. Hultman, U. Helmersson, J.-E. Sundgren, J. E. Greene, *Thin Solid Films* 169 (1989) 299.

[6] T. -Y. Lee, S. Kodambaka, J. G. Wen, R. Twesten, J. E. Greene, and I. Petrov, *Appl. Phys. Lett*., 84 (2004) 2796.

[7] B. W. Karr, Y. W. Kim, I. Petrov, D. B. Bergstrom, D. G. Cahill, and J. E. Greene, *J. Appl. Phys.* 80 (1996) 6699.

[8] J.E. Greene, "Nucleation, Growth, and Microstructural Evolution in Films Grown by Physical Vapor Deposition," in *Deposition Technologies for Films and Coatings*, ed. by R.F. Bunshah, Noyes Publications, Park Ridge, NJ (1994), p. 681.

[9] L. Hultman, J.‐E. Sundgren, J. E. Greene, D. B. Bergstrom, and I. Petrov, *J. Appl. Phys*. 78 (1995) 5395.

[10] J. E. Greene, J.‐E. Sundgren, L. Hultman, I. Petrov, and D. B. Bergstrom, *Appl. Phys. Letters* 67 (1995) 2928.

[11] J.E. Greene, "Thin Film Nucleation, Growth, and Microstructural Evolution: an Atomic Scale View," in *Handbook of Deposition Technologies for Thin Films and Coatings*, Third Edition, ed. by P. Martin, William Andrew Publications (Elsevier), Burlington, MA (2010).

[12] J.A. Thornton and D.W. Hoffman, *Thin Solid Films* 171 (1989) 5.

[13] I. Petrov L. Hultman J.‐E. Sundgren, J. E. Greene, *J. Vac. Sci. Technol. A* 10 (1992) 265.

[14] G. Greczynski, J. Lu, I. Petrov, J.E. Greene, S. Bolz, W. Kölker, Ch. Schiffers, O. Lemmer and L. Hultman, *J. Vac. Sci. Technol. A* 32 (2014) 041515.

[15] G. Greczynski, J. Lu, J. Jensen, I. Petrov, J.E. Greene, S. Bolz, W. Kölker, Ch. Schiffers, O. Lemmer and L. Hultman, *J. Vac. Sci. Technol. A* 30 (2012) 061504.

[16] G. Greczynski, J. Lu, M. Johansson, J. Jensen, I. Petrov, J.E. Greene, and L. Hultman, *Surf. Coat. Technol*. 206 (2012) 4202.

[17] G. Greczynski, J. Lu, M. Johansson, J. Jensen, I. Petrov, J.E. Greene, and L. Hultman, *Vacuum* 86 (2012) 1036.

[18] J.M.E. Harper, J.J. Cuomo, R. J. Gambino, and H. R. Kaufman, in Ion Bombardment Modification of Surfaces, edited by O. Auciello and R. Kelly (Elsevier, New York, 1984). Chap. 4.

[19] V. Poulek, J. Musil, V. Valvoda, and R. Kuzel, *Thin Solid Films* 196 (1991) 265.

[20] G. Greczynski, J. Lu, J. Jensen, I. Petrov, J.E. Greene, S. Bolz, W. Kölker, Ch. Schiffers, O. Lemmer and L. Hultman, *Thin Solid Films* 556 (2014) 87.

[21] G. Greczynski, J. Lu, J. Jensen, S. Bolz, W. Kölker, Ch. Schiffers, O. Lemmer, J.E. Greene, and L. Hultman, *Surf. Coat. Technol*. 257 (2014) 15.

[22] A. Flink, M. Beckers, J. Sjölén, T. Larsson, S. Braun, L. Karlsson, L. Hultman, *J. Mater. Res*. 24/8 (2009) 2483.

[23] A.O. Eriksson, O. Tengstrand, J. Lu, J. Jensen, P. Eklund, J. Rosén, I. Petrov, J.E. Greene, and L. Hultman, *Surf. Coat. Technol*. 257 (2014) 121.

[24] H. Söderberg, M. Odén, A. Flink, J. Birch, P.O.Å. Persson, M. Beckers, L. Hultman, *J. Mater. Res.* 22/11 (2007) 3255.

[25] L. Hultman, J. Bareño, A. Flink, H. Söderberg, K. Larsson, V. Petrova, M. Odén, J.E. Greene, I. Petrov, *Phys. Rev. B*, 75 (2007) 155437.

[26] J. Patscheider, N. Hellgren, R.T. Haasch, I. Petrov, and J.E. Greene, *Phys. Rev. B* 83 (2011) 125124.

[27] S. Veprek, *J. Vac. Sci. Technol. A* 17 (1999) 2401-2420.

[28] S. Li, Y. Shi and H. Peng, *Plasma Chem. Plasma Process.* 12 (1992) 287.

[29] S. Veprek, S. Reiprich, *Thin Solid Films* 268 (1995) 64.

[30] S. Veprek, *J. Vac. Sci. Technol. B* 20 (2002) 650.

[31] J. Patscheider, T. Zehnder, M. Diserens, *Surf. Coat. Technol.* 146-147 (2001) 201.

[32] F. Vaz, L. Rebouta, S. Ramos, M.F. da Silva, J.C. Soares, *Surf. Coat. Technol.* 108–109 (1998) 236.

[33] M. Diserens, J. Patscheider, F. Lévy, *Surf. Coat. Technol*. 108–109 (1998) 241.

[34] P. Jedrzejowski, J.E. Klemberg-Sapieha, L. Martinu, *Thin Solid Films* 426 (2003) 150–159.

[35] A. Flink, T. Larsson, J. Sjölén, L. Karlsson, L. Hultman, *Surf. Coat. Technol.* 200 (2005) 1535.

[36] T. Marten, E. I. Isaev, B. Alling, L. Hultman, and I. A. Abrikosov *Phys. Rev. B* 81 (2010) 212102.

[37] V. I. Ivashchenko, S. Veprek, P.E.A. Turchi, V.I. Shevchenko *Phys. Rev. B* 85 (2012) 195403.

[38] V.I. Ivashchenko, S. Veprek, A.S. Argon, P.E.A. Turchi, L. Gorb, F. Hill, J. Leszczynski, *Thin Solid Films* 578 (2015) 83.

[39] T. Marten, B. Alling, E.I. Isaev, H. Lind, F. Tasnádi, L. Hultman, and I.A. Abrikosov *Phys. Rev. B* 85 (2012) 104106.
[40] S. Hao, B. Delley, S. Veprek, and C. Stampfl, *Phys. Rev. Lett.* 97 (2006) 086102.
[41] B. Alling, E. I. Isaev, A. Flink, L. Hultman, and I. A. Abrikosov *Phys. Rev. B* 78 (2008) 132103.
[42] http://www.cemecon.de/coating_technology/coating_units/hipims_sputter_coating_system/index_eng.html, accessed in February 2015
[43] D.J. Christie, *J. Vac. Sci. Technol. A* 23 (2005) 330.
[44] G. Greczynski, J. Jensen, J. Böhlmark, L. Hultman, *Surf. Coat. Technol.* 205 (2010) 118.
[45] G. Greczynski and L. Hultman, *Vacuum* 84 (2010) 1159.
[46] J. Jensen, D. Martin, A. Surpi, T. Kubart, *Nucl. Instr. Meth. B* 268 (2010) 1893.
[47] see, e.g., chapter 6 in M. Birkholz *Thin Film Analysis by X-ray Scattering*, ISBN-10: 3-527-31052-5, Wiley-VCH, Weinheim 2006
[48] W. C. Oliver and G. M. Pharr, *J. Mater. Res.* 7 (1992) 1564.
[49] J. F. Ziegler, J. P, Biersack, U. Littmark, "The Stopping and Range of Ions in Solids," vol. 1 of series "Stopping and Ranges of Ions in Matter," Pergamon Press, New York (1984).
[50] www.srim.org; accessed on 2013-06-28.
[51] P.E. Blöchl, *Phys. Rev. B* 50 (1994) 17953.
[52] G. Kresse and J. Hafner, *Phys. Rev. B* 48 (1993) 13115.
[53] G. Kresse and D. Joubert, *Phys. Rev. B* 59 (1999) 1758.
[54] J.P. Perdew, K. Burke, M. Ernzerhof, *Phys. Rev. Lett.* 77 (1996) 3865.
[55] A. Zunger, S.-H. Wei, L.G. Ferreira, and J.E. Bernard, *Phys. Rev. Lett.* 65 (1990) 353.
[56] B. Alling, A.V. Ruban, A. Karimi, O. E. Peil, S.I. Simak, L. Hultman, and I. A. Abrikosov, *Phys. Rev. B* 75 (2007) 045123.
[57] J. F. Nye, Physical Properties of Crystals: Their Representation by Tensors and Matrices (Oxford University Press, USA, 1985).
[58] L. Vitos, Computational Quantum Mechanics for Materials Engineers: The EMTO Method and Applications (Engineering Materials and Processes) (Springer, Berlin, 2010).
[59] F. Tasnádi, M. Odén, and I. A. Abrikosov, *Phys. Rev. B* 85 (2012) 144112.
[60] G. Simmons, H. Wang, Single Crystal Elastic Constants and Calculated Aggregate Properties: A Handbook, M.I.T Press, Cambridge, 1971
[61] G. Greczynski, J. Jensen, L. Hultman, *IEEE Transactions on Plasma Science* 38 (2010) 3046.
[62] G. Greczynski, J. Jensen, L. Hultman, *Thin Solid Films* 519 (2011) 6354.
[63] The JCPDS database (1998), data set number: 38-1420; W. Wong-Ng, H. McMurdie, B. Paretzkin, C. Hubbard, A. Dragoo, *Powder Diffraction* 2 (1987) 2.
[64] B. Alling, P. Steneteg, C. Tholander, F. Tasnádi, I. Petrov, J.E. Greene, L. Hultman, *Phys. Rev. B* 85 (2012) 245422.
[65] O. Tengstrand, N. Nedfors, B. Alling, U. Jansson, A. Flink, P. Eklund, L. Hultman, *Surf. Coat. Technol* 258 (2014) 392.
[66] C. Stampfl,W. Mannstadt, R. Asahi, and A. J. Freeman, *Phys. Rev. B* 63 (2001) 155106.
[67] I. Petrov, A. Myers, J.E. Greene, J.R. Abelson *J. Vac. Sci. Technol. A* 12 (1994) 2846.
[68] David R. Lide (ed), *CRC Handbook of Chemistry and Physics, 84th Edition*. CRC Press. Boca Raton, Florida, 2003; Section 10, Atomic, Molecular, and Optical Physics; Ionization Potentials of Atoms and Atomic Ions.
[69] D. J. Kester and R. Messier, *J. Appl. Phys*. 72 (1992) 504.
[70] I. Petrov, F. Adibi, J.E. Greene, W.D. Sproul, and W.-D. Munz, *J. Vac. Sci. Technol. A* 10 (1992) 3283.
[71] I.G. Brown and X. Godechot, *IEEE Trans. Plasma Sci*. 19 (1991) 713.